ALMA MATER STUDIORUM
UNIVERSITÀ DI BOLOGNA

DEPARTMENT OF BIOLOGICAL, GEOLOGICAL AND ENVIRONMENTAL SCIENCES

SECOND CYCLE DEGREE

ENVIRONMENTAL ANALYSIS AND MANAGEMENT

# A MACHINE LEARNING APPROACH FOR COASTAL WATER QUALITY RETRIEVAL USING SATELLITE IMAGES: THE CASE OF THE ROMAGNA COAST

Dissertation in Coastal Geomorphology and Remote Sensing

**Supervisor**

**Prof. Sonia Silvestri**

**Co-Supervisor**

**Dr. Milad Niroumand-Jadidi**

**Defended by**

**Yuqiao Chen**

**Graduation Session / March/ 2026**

**Academic Year 2024/2025**

# Abstract

Monitoring water quality in the coastal waters of the Emilia-Romagna region (Northern Adriatic Sea) represents a formidable challenge for satellite remote sensing. The Po River plume creates a dynamic Case-2 environment where phytoplankton, suspended particulate matter, and colored dissolved organic matter (CDOM) co-vary independently. These conditions frequently compromise the reliability of traditional retrieval algorithms and standard land-oriented atmospheric correction procedures.

This study develops and validates a neural network (MLP) framework to retrieve Chlorophyll-a and Turbidity from Sentinel-2 MSI and Landsat-8/9 OLI imagery (2020–2023). Utilizing in-situ data from two fixed monitoring stations, a Bayesian hyperparameter optimization framework was employed to identify robust model architectures. To evaluate the methodological necessity of atmospheric correction in turbid waters, models were trained and compared using both Top-of-Atmosphere (TOA) and Surface Reflectance (SR) products.

Results indicate that Sentinel-2 systematically outperforms Landsat-8/9, an advantage primarily driven by its dedicated red-edge spectral bands and finer spatial resolution. More critically, the study finds that models trained directly on TOA reflectance consistently match or exceed the performance of SR-based models. This suggests that neural networks can implicitly compensate for atmospheric effects, bypassing the systematic biases often introduced by standard correction processors in turbid nearshore zones. High-resolution spatiotemporal maps generated from the optimized models successfully captured regional hydrodynamic features, including current-driven plume confinement and seasonal biomass shifts.

These findings demonstrate that TOA-based neural network modelling offers a more resilient and practical alternative for operational water quality monitoring in complex coastal environments where standard atmospheric correction remains a significant source of uncertainty.



**Keywords:** Coastal water quality; Case-2 waters; Chlorophyll-a; Turbidity; Neural networks; Machine learning; Bayesian optimization; Top-of-Atmosphere (TOA); Atmospheric correction; Northern Adriatic Sea; Sentinel-2; Landsat-8/9.

# Table of Contents

# Chapter 1 Introduction

## 1.1 Background

Coastal areas represent the highly populous and economically active regions globally. Recent geospatial analysis indicates that as of 2018, approximately 2.86 billion people—nearly 40% of the global population—reside within a 100 km buffer of the shoreline, with densities averaging twice the global mean (Creel, 2003; Cosby et al., 2024). The annual economic value of the ocean, if ranked as a nation, would stand as the world's seventh-largest economy with an annual gross marine product exceeding US$2.5 trillion (Hoegh-Guldberg et al., 2015). This economic vitality is underpinned by a disproportionately high biological productivity. Although coastal waters cover less than 10% of the global ocean surface, they are disproportionately productive, accounting for approximately 25% of total marine primary production (Berger et al., 1989). However, this prosperity is fragile. More than two-thirds of the ocean's annual economic value relies directly on maintaining healthy, functioning ocean ecosystems (Hoegh-Guldberg et al., 2015).

Due to intensifying anthropogenic pressures (industrialization, tourism) and the compounding effects of climate change, coastal water quality faces significant deterioration, especially regarding eutrophication. According to recent global assessments, the expansion of agriculture and urbanization has dramatically increased nutrient loading to coastal zones, identifying cultural eutrophication as a primary driver of ecosystem degradation (Malone and Newton, 2020). This challenge is further compounded by ocean warming, which reduces oxygen solubility and enhances stratification, thereby increasing the vulnerability of coastal systems to deoxygenation and dead zones (Breitburg et al., 2018). In shallow, semi-enclosed basins like the Northern Adriatic, these synergistic effects are particularly acute, threatening both biodiversity and the marine economy (Malone and Newton, 2020; Vona et al., 2025). Thus, continuous and precise monitoring is vital for protecting both ecosystem and public health.

## 1.2 Challenges in Satellite Optical Remote Sensing of Coastal Waters

Effective implementation of environmental directives, such as the Marine Strategy Framework Directive (MSFD) and Water Framework Directive (WFD), require continuous and comprehensive monitoring strategies. While traditional in-situ sampling provides high accuracy, it is often limited by poor spatiotemporal coverage and high operational costs, making it insufficient to capture the rapid dynamics of coastal waters (Adjovu et al., 2023). In this context,

satellite Ocean Colour (OC) remote sensing has emerged as a unique tool, offering a synoptic view for detecting large-scale biogeochemical patterns (Kwong et al., 2022; Mohseni et al., 2022; Adjovu et al., 2023). However, exploiting this potential in optically complex coastal waters requires addressing several fundamental technical challenges.

A fundamental challenge in satellite optical remote sensing of water bodies stems from their inherently low reflectance. Water acts as a dark object, absorbing the majority of incident solar radiation, such that water-leaving radiance constitutes only a small fraction of the total signal recorded at the top of the atmosphere (TOA). The remaining signal is dominated by atmospheric path radiance arising from Rayleigh scattering and aerosol interactions, resulting in a low signal-to-noise ratio (SNR) over water surfaces (Brockmann et al., 2016; Niroumand-Jadidi et al., 2022). Atmospheric correction (AC) is therefore a critical pre-processing step, aiming to isolate the water-leaving reflectance from the TOA signal. However, in optically turbid nearshore waters, existing AC algorithms are subject to significant uncertainties, as the assumptions underpinning their aerosol characterisation are often violated under high sediment and CDOM loading conditions (Vanhellemont and Ruddick, 2021; Zhang et al., 2023). This raises the question of whether machine learning models trained directly on TOA reflectance can implicitly account for atmospheric effects, potentially bypassing the errors introduced by imperfect atmospheric correction — a question this study directly addresses.

However, applying remote sensing in transitional coastal zones presents unique optical challenges. Unlike open oceans (Case-1 waters) where optical properties are determined solely by phytoplankton, coastal regions are typically Case-2 waters, characterized by a complex optical interplay of phytoplankton, suspended sediments, and Colored Dissolved Organic Matter (CDOM) (Kyryliuk and Kratzer, 2019).

The Northern Adriatic Sea serves as a prime example of this complexity. As the largest river in Italy, the Po River contributes a significant portion of the freshwater runoff into the basin, introducing massive loads of suspended solids and nutrients (Mikhailova, 2002; Brando et al., 2015). The dispersion of this plume is further modulated by the West Adriatic Coastal Current (WACC) and local wind regimes (Bora and Scirocco), creating a highly dynamic and optically turbid environment that renders traditional Case-1 algorithms ineffective (Manzo et al., 2018).

Consequently, standard empirical algorithms often fail to resolve such complex signals. As highlighted by Matsushita et al. (2012), standard algorithms developed for Case-1 waters

yield inaccurate estimates in Case-2 environments because the independent variations of sediments and CDOM violate the bio-optical assumptions of simple band-ratios. Berthon and Zibordi (2004) observed that standard band-ratio algorithms (e.g., OC2v4) tend to systematically overestimate chlorophyll-a concentrations in the Northern Adriatic Sea, due to the strong absorption of the blue part of the spectrum by dissolved and particulate matter.

### 1.3 Water Quality Retrieval Algorithms: Review and Limitations

To address the limitations of empirical band-ratio algorithms in Case-2 waters, physics-based approaches have been developed that invert radiative transfer models accounting for the absorption and backscattering properties of water constituents, including Chl-a, TSM, and CDOM. Widely used processors such as the Case-2 Regional CoastColour (C2RCC) and the Water Colour Simulator (WASI) represent two main paradigms: look-up table (LUT)-based inversion and analytical spectrum matching, respectively (Gege, 2014; Brockmann et al., 2016; Niroumand-Jadidi et al., 2022; Niroumand-Jadidi and Gege, 2025). While physics-based approaches do not rely on concurrent in-situ measurements for training, they present their own limitations. LUT-based models such as C2RCC are sensor-specific and cannot be adapted to site-specific bio-optical conditions, limiting their applicability in highly dynamic environments like the Northern Adriatic (Niroumand-Jadidi and Gege, 2025). Analytical approaches such as WASI offer greater flexibility but are computationally prohibitive for routine image processing over large areas (Niroumand-Jadidi and Gege, 2025).

To overcome the optical complexity of the Po River plume and the inter-sensor inconsistencies, Machine Learning (ML) approaches, particularly neural networks (NNs), have emerged as a promising alternative, capable of capturing the complex non-linear relationships between satellite reflectance and water quality parameters without requiring explicit knowledge of the underlying bio-optical physics (Manzo et al., 2018; Adjovu et al., 2023; Niroumand-Jadidi et al., 2022). However, empirical ML models are fundamentally constrained by the availability and representativeness of in-situ training data. Field measurements must be acquired concurrently with satellite overpasses and must adequately represent the bio-optical variability of the water body, making these models largely image-specific with limited spatiotemporal transferability (Politi et al., 2015; Niroumand-Jadidi et al., 2022; Niroumand-Jadidi and Gege, 2025). In the context of this study, the available in-situ dataset is derived from fixed moored sensors rather than spatially distributed field campaigns, introducing additional challenges. The temporal nature of these measurements means that the training data inevitably

captures variations in bio-optical conditions driven by Po River discharge events and seasonal dynamics, fluctuations in atmospheric state across different satellite overpasses, and potential measurement noise introduced by sensor biofouling and calibration drift. These factors collectively increase the complexity of model training and underscore the need for robust validation strategies.

To resolve these highly dynamic features, a single satellite mission is often inadequate. Landsat-8 offers the necessary spatial resolution (30 m) to resolve near-shore plumes (Roy et al., 2014), and together with the recently launched Landsat-9, they provide an 8-day revisit cycle to enhance the temporal frequency of coastal monitoring (Niroumand-Jadidi et al., 2022). Sentinel-2 provides higher frequency (5 days) and finer resolution (10–20 m) but differs slightly in spectral configuration (Drusch et al., 2012). The combined use of both sensors therefore enhances the temporal resolution of coastal monitoring.

### 1.4 Research Objectives

Despite the demonstrated potential of machine learning approaches for water quality retrieval in optically complex waters, their application in environments characterised by temporally-measured, fixed-sensor in-situ data — such as the Romagna coast — remains insufficiently explored. In particular, the relative performance of models trained on TOA versus atmospherically corrected surface reflectance in turbid nearshore waters, where atmospheric correction uncertainties are substantial, has not been systematically evaluated.

This study therefore pursues the following objectives:

1. To develop and optimize a Neural Network model using Bayesian hyperparameter tuning for accurate retrieval of Chl-a and Turbidity in optically complex coastal waters.
2. To assess the consistency and applicability of Landsat-8/9 and Sentinel-2 sensors for coastal water quality monitoring, and evaluate the effect of atmospheric correction on model performance by comparing TOA and surface reflectance inputs.
3. To generate high-resolution spatiotemporal distribution maps of Chl-a and Turbidity along the Romagna coast to support environmental management and analyse Po River plume dynamics.

### 1.5 Thesis Structure

The remainder of this thesis is organised as follows. Chapter 2 describes the study area, the bio-optical characteristics of the Romagna coast, the multi-mission satellite and in-situ datasets

utilised, and the methodology including data pre-processing, spatiotemporal match-up strategy, and the Bayesian optimisation workflow for model development. Chapter 3 presents the algorithm performance evaluation and the spatiotemporal distribution maps of water quality derived from the satellite time-series. Chapter 4 discusses the results in the context of the broader literature and addresses the limitations of the study. Finally, Chapter 5 summarises the main conclusions and suggests directions for future research.

# Chapter 2 Methodology

## 2.1 Study Area: The Emilia-Romagna Coastal Zone

### *2.1.1 Geography and Geomorphology*

The Emilia-Romagna coastal waters are located along the western Northern Adriatic Sea (NAS). The NAS is a semi-closed sub-basin with an average depth of 35 meters - the shallowest part of the Adriatic Sea (Vona et al., 2025). It features a gently sloping seabed and a sandy coastline. The study area extends from the Po River Delta in the north to the southern boundary of the Romagna coast (Figure 2.1).

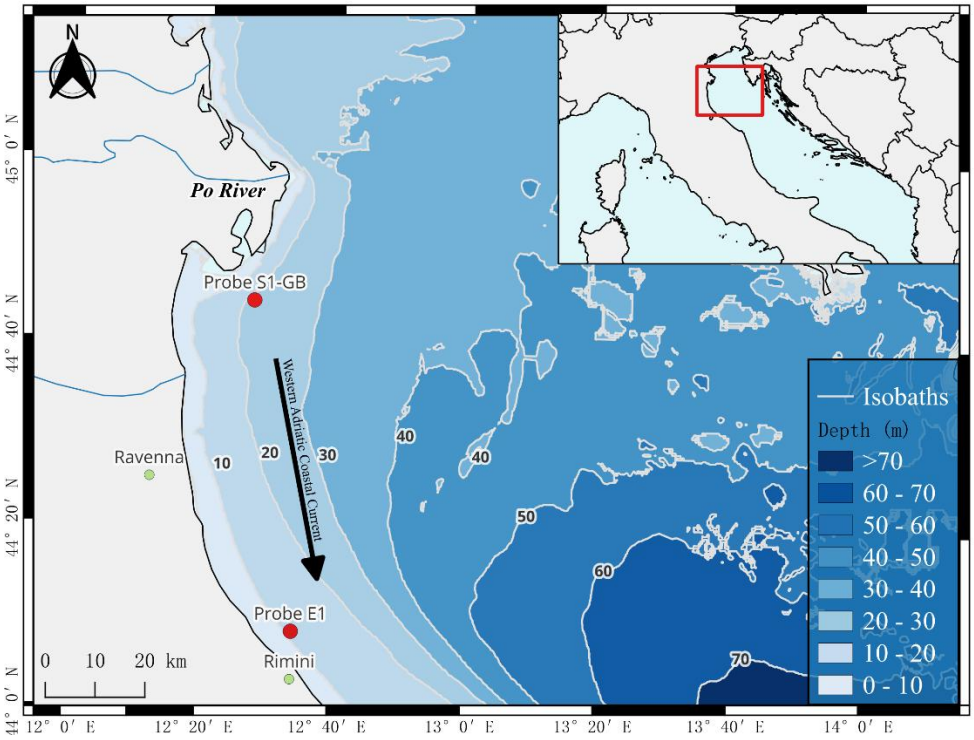


*Figure 2.1 Map of the study area along the Emilia-Romagna coastal zone. Bathymetry (blue shading) highlights the topography of the basin. Red points indicate the oceanographic monitoring stations S1 and E1. The black arrow represents the main direction of the Western Adriatic Coastal Current (WACC). (Data sources: EMODnet Bathymetry and CNR-ISMAR).*

### *2.1.2 Influence of the Po River*

The NAS basin is significantly influenced by river inputs, with the Po River acting as the most prominent contributor of freshwater and nutrients in this region. It has a long-term average discharge of 1,511 $m^3/s$, which varies significantly seasonally, with two distinct peaks: a spring (May–June) peak driven by snowmelt, and an autumnal (October–November) peak resulting from intense rainfall. Additionally, the Po River is a major source of eutrophication,

contributing more than 50% of the total nutrient load to the NAS (Degobbis and Gilmartin, 1990; Boldrin et al., 2005; Falcieri et al., 2014).

Recent research conducted by Vona et al. (2025) shows a positive correlation between the Po River discharge and the spatiotemporal trends of both Chlorophyll-a and Total Suspended Matter (TSM), confirming the river's dominant role in modulating water quality dynamics in the basin. Braga et al. (2017) also found out that the massive input by the Po River resulted in extremely high turbidity patterns in the region, making this coastal area a highly optically complex body of water.

### *2.1.3 Circulation and Wind Regimes*

Besides riverine impacts, the circulation along the Romagna coast is also impacted by the Western Adriatic Coastal Current (WACC), a southward flowing coastal current along the western side of the basin. It is the main force that carries suspended matter along the Adriatic Sea Italian coast (Vona et al., 2025). Moreover, the local hydrodynamics are strongly modulated by two opposing wind regimes, the northeastern wind Bora and the southeastern wind Sirocco, which represent the strongest wind forcing in the Adriatic area. These winds significantly influence the circulation patterns and the transportation of riverine materials within the basin. (Orlić, Kuzmić and Pasarić, 1994)

## 2.2 Data Acquisition and Pre-processing

To characterize the spatiotemporal variability of water quality parameters in the Emilia-Romagna coastal zone, this study combines multi-sensor satellite observations from the Sentinel-2 *Multispectral* Instrument (MSI) and the Landsat-8/9 Operational Land Imager (OLI/OLI-2). Leveraging the complementary revisit cycles of these missions enhances the effective temporal resolution of the dataset, which is essential for resolving rapid changes in highly dynamic coastal waters. In support of algorithm application, high-frequency in-situ measurements from fixed oceanographic monitoring platforms are used to calibrate and validate the satellite-derived retrievals, providing an independent reference for key water quality parameters.

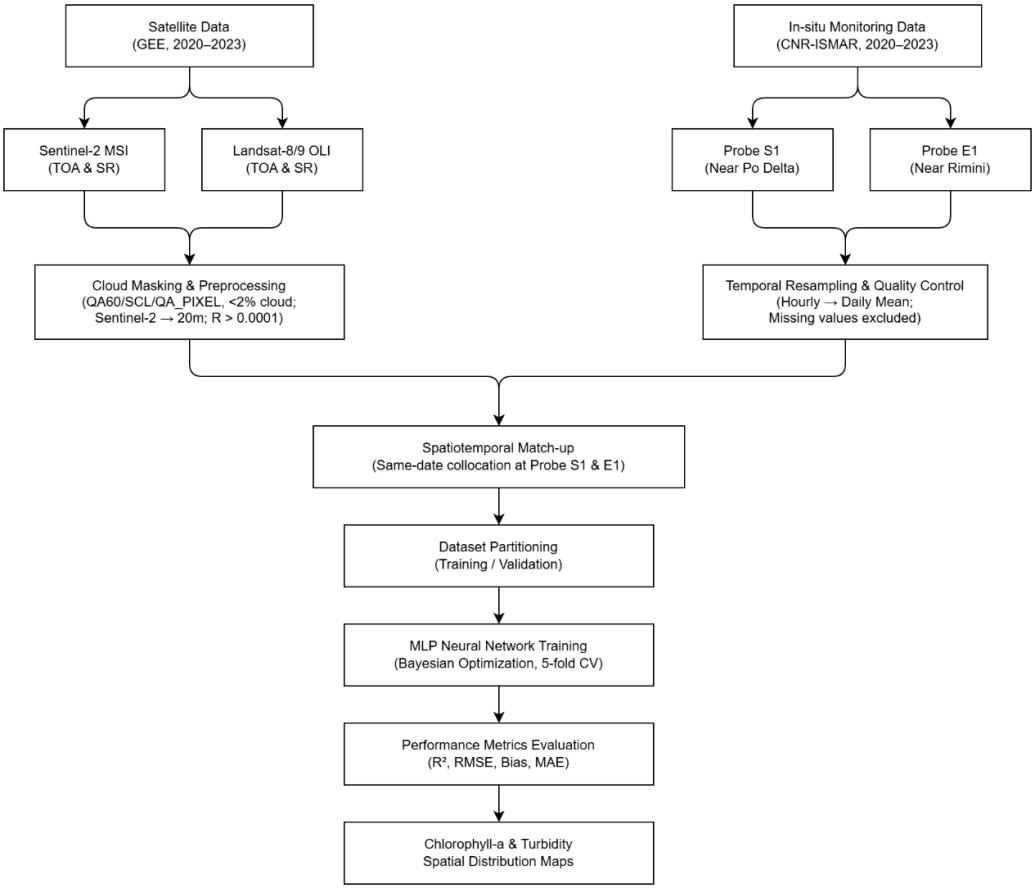


*Figure 2.2 Schematic overview of the research methodology workflow.*

### *2.2.1 In-situ Monitoring Data Acquisition and Preprocessing*

The in-situ data were obtained from two fixed monitoring stations (see Figure 2.1 for their locations) operated by the Institute of Marine Sciences of the National Research Council (CNR-ISMAR) along the Romagna coast in the Northern Adriatic Sea: Probe S1 (Meda S1-GB) (http://s1.bo.ismar.cnr.it/perl/s1_home.pl) and Probe E1 (Boa Meteo-Oceanografica E1) (http://e1.bo.ismar.cnr.it/perl/e1_home.pl). These autonomous platforms provide continuous measurements of physical, chemical, and biological parameters to support oceanographic modeling and environmental monitoring. Detailed specifications of the stations are summarized in Table 2.1 and Table 2.2.

*Table 2.1 Geographic Information of In-situ Monitoring Stations*

| Probe Name | Coordinates (Lat, Lon) | Distance from Coast | Seabed Depth (m) |
|---|---|---|---|
| Probe S1 (Meda S1-GB) | 44.7385°N, 12.454°E | ~4 nm south of Po di Goro mouth (Po Delta) | 22.5 |
| Probe E1 (Boa E1) | 44.143°N, 12.57°E | ~4 nm north of Rimini | 10.5 |

*Table 2.2 Measurement Configuration and Study Period of Monitoring Stations*

| Probe Name | Measurement Depths (m) | Key Measured Variables | Study Period |
|---|---|---|---|
| Probe S1 (Meda S1-GB) | -2.5(used) and -18.5 | Chl-a fluorescence (mg/m³), Turbidity (NTU), Salinity (PSU), etc. | 2020-01-01 to 2023-12-31 |
| Probe E1 (Boa E1) | -1.6(used) and -8.0 | Same as Probe S1 | Same as Probe S1 |

*Note: The information from CNR-ISMAR official website. Seabed depths are nominal installation values; actual water depth may vary slightly due to sedimentation. Measurements are taken continuously at two depths using autonomous sensors, Only the near-surface depth (-2.5 m and -1.6 m, respectively) is used in this study; the deeper measurements (-18.5 m and -8.0 m) are excluded from analysis.*

For this research, in-situ Chlorophyll-a fluorescence (F-CHL, mg/m³) and Turbidity (TURB, NTU) were selected as target variables for neural network training and validation. The raw hourly observations were temporally resampled to daily mean values using arithmetic averaging to ensure compatibility with discrete satellite overpasses and to mitigate high-frequency fluctuations from surface waves, tides, or instrument noise. Days with missing daily means for turbidity or Chlorophyll-a were excluded from the match-up dataset.

### *2.2.2 Satellite Data Acquisition and Preprocessing*

All satellite data retrieval and preprocessing operations were carried out using the Google Earth Engine (GEE) cloud computing platform. Both Surface Reflectance (SR) and Top-of-Atmosphere (TOA) products were obtained from the Sentinel-2 (MSI) and Landsat-8/9 (OLI/OLI-2) missions for subsequent algorithm application and inter-sensor comparison. The analysis workflow covered the period from January 1, 2020, to December 31, 2023, consistent with the temporal extent of the available in-situ measurements. The preprocessing pipeline comprised cloud and quality masking (applied to both sensors), spatial harmonization of Sentinel-2 bands to a uniform 20 m resolution, and radiometric filtering of near-zero water reflectance.

*Table 2.3 Specifications of Satellite Sensors Used in the Study*

| Satellite | Sensor | Extracted Bands | Spatial Resolution | Revisit Cycle |
|---|---|---|---|---|
| Sentinel-2 (A/B) | MSI (Multispectral Instrument) | B1, B2, B3, B4, B5, B6, B7, B8, B8A | Native: 10/20/60 m (resampled to 20m) | 5 days (combined constellation) |
| Landsat-8/9 | OLI / OLI-2 (Operational Land Imager) | B1, B2, B3, B4, B5, B6, B7 | 30 m | 8 days (combined constellation) |

Cloud contamination represents a fundamental challenge in optical remote sensing of coastal waters. For Sentinel-2 imagery, the QA60 bitmask (TOA) and Scene Classification Layer (SCL, SR) were combined with the S2Cloudless probability layer (threshold < 20 %) to identify and mask opaque clouds, cirrus clouds, and cloud shadows. For Landsat-8/9, the QA_PIXEL quality assessment band was used to flag and remove pixels affected by clouds, dilated cloud features, and shadows. In addition, for every overpass, a local cloud fraction was calculated inside a 20 × 20-pixel window (400 m for Sentinel-2 at 20 m resolution; 600 m for Landsat at 30 m) centered on each probe. Images were retained only if the cloud cover within this window was strictly less than 2 % and at least 50 % of the pixels were valid in the cloud-filtering window.

Given that Sentinel-2 spectral bands possess varying native spatial resolutions (B1 at 60 m, B2–B4 and B8 at 10 m, B5–B7 and B8A at 20 m), all Sentinel-2 bands were resampled to a uniform 20 m resolution using bilinear interpolation. Landsat-8/9 bands remained their native 30 m resolution. For each retained image, mean reflectance values were computed within a 5 × 5-pixel window (Sentinel-2, 100 m × 100 m) and a 3 × 3-pixel window (Landsat-8/9, 90 m × 90 m) centered on the probe location. To ensure data quality, only images where at least 50 % of the pixels within this extraction window were valid and all pixel values were positive were retained.

For Sentinel-2 data, samples in which the mean reflectance in any of the extracted bands within the extraction window was less than or equal to 0.0001 were discarded prior to model training and validation. This value represents a single quantization step above zero in the Sentinel-2 L2A product (European Space Agency, 2024), where the absolute radiometric uncertainty (~0.005) is approximately two orders of magnitude larger than the signal itself. At this level, measured values are expected to be dominated by quantization noise and residual atmospheric correction errors rather than physical water-leaving radiance. This filtering criterion is consistent with standard quality control protocols that reject spectra with near-zero or negative remote sensing reflectance values (Bailey and Werdell, 2006; Pahlevan et al., 2022).

### *2.2.3 Spatiotemporal Match-up Strategy*

Satellite spectral reflectance values were extracted at the coordinates of Probe S1 and Probe E1 using the spatial windowing approach described in Section 2.2.2. This method ensures comparable sampling scales across sensors despite differing native resolutions, while effectively filtering out invalid or noisy pixels.

Temporal collocation was achieved by pairing each satellite overpass with the daily mean in-situ values of Chlorophyll-a and Turbidity recorded on the same calendar day, ensuring compatibility between near-instantaneous satellite acquisitions and the continuous in-situ time series.

Comprehensive match-up datasets were generated for SR and TOA products of both missions. Landsat-8 and Landsat-9 observations were pooled into a single dataset given their identical spectral band designations (B1–B7) and high inter-sensor consistency, as both satellites were designed to operate as a coordinated constellation. Sentinel-2 data were kept as a separate dataset throughout the analysis. Overlapping Sentinel-2 tiles near Probe E1 were averaged during preprocessing for consistency. All matchups underwent final quality screening, excluding cases with missing in-situ values. This strategy balances data quantity with reliability, accommodating the high spatiotemporal variability of coastal waters in the Emilia-Romagna region.

## 2.3 Neural Network-Based Regression Model Application

### *2.3.1 Model Architecture and Input Configuration*

To retrieve water quality parameters (Chlorophyll-a concentration and turbidity) from multi-sensor satellite imagery, a feed-forward Multi-Layer Perceptron (MLP) neural network architecture was employed, adapted from the regression-based neural network framework developed by Niroumand-Jadidi et al. (2022a, 2022b, 2025) and implemented using code provided by the co-supervisor. MLPs are highly effective in modeling the complex, non-linear relationships between satellite reflectance and aquatic biogeochemical properties, often outperforming traditional band-ratio models like OBRA (Legleiter et al., 2009) in water constituent and bathymetry retrieval (Niroumand-Jadidi et al., 2022a).

For Sentinel-2 MSI data, the input layer consisted of nine spectral bands: the Coastal Aerosol band (B1), visible spectrum bands (B2–B4), Red-Edge bands (B5–B7), and Near-Infrared bands (B8, B8A). For Landsat-8/9 OLI data, seven spectral bands were used as inputs: Coastal/Aerosol (B1), visible bands (B2–B4), Near-Infrared (B5), and two Short-Wave Infrared bands (B6, B7). Separate models were trained for each target variable and sensor-product configuration.

### *2.3.2 Data Transformation and Preprocessing*

The application of $\log_{10}$ transformation of Chl and turbidity field measurements was determined empirically through preliminary training experiments. For each dataset, the model was first trained in linear space; where this approach yielded poor convergence or substantially biased predictions, $\log_{10}$ transformation of the target variable was subsequently applied. Through this process, a consistent pattern emerged: $\log_{10}$ transformation was beneficial for all TOA-based Chlorophyll-a models (both Sentinel-2 and Landsat-8/9), while the SR-based models trained in linear space yielded adequate performance without transformation. This difference likely reflects the more complex, non-linear relationship between TOA reflectance and water quality constituents due to residual atmospheric signal. Additionally, $\log_{10}$ transformation was applied to the Landsat-8/9 SR turbidity dataset at Probe S1, which is subject to the most extreme concentration fluctuations near the Po river mouth. For all log-transformed models, predictions were back-transformed to linear space (10^x) prior to accuracy assessment.

### *2.3.3 Bayesian Optimization for Hyperparameter Tuning*

The architecture and learning capacity of an MLP are highly sensitive to its hyperparameters. To ensure an optimal network configuration without manual trial-and-error, an automated Bayesian Optimization was implemented via MATLAB's fitrnet function with the OptimizeHyperparameters interface. The Expected Improvement Plus (expected-improvement-plus) acquisition function was utilized to efficiently explore the hyperparameter space over a maximum of 40 objective evaluations.

To prevent overfitting, the objective function was minimized using a 5-fold cross-validation strategy on the training dataset. A random seed of 13 was set for reproducibility. The Bayesian optimization dynamically tuned the following key hyperparameters:

- Network Depth and Width: The number of hidden layers was constrained between 1 and 3, with the number of neurons per layer allowed to range from 1 to 50 (Layers 1 and 2) and 1 to 30 (Layer 3).
- Activation Functions: The algorithm selected the optimal non-linear activation function from Rectified Linear Unit (ReLU), Hyperbolic Tangent (Tanh), and Sigmoid.
- Regularization and Standardization: The L2 regularization strength was tuned within a range of 10^{-5} to 1 to penalize excessive network complexity, while the necessity of input feature standardization was also treated as a tunable parameter.

*2.3.4 Training and Validation Dataset Division*

Validation was restricted to same-date matchups between Landsat and Sentinel-2 observations. These temporally coincident pairs provide independent but environmentally comparable data for rigorous inter-sensor validation. All remaining matchups were allocated to training, ensuring strict temporal independence while maximizing the training sample size.

*2.3.5 Model Performance Metrics*

The predictive performance of the optimized neural networks was assessed on the independent validation dataset using both linear and log-transformed metrics. Consistent with standard ocean color evaluation protocols, the coefficient of determination ($R^2$) and Root Mean Square Error (RMSE) were calculated in linear space as follows:

$$R^2 = 1 - \frac{\sum_{i=1}^{N}(y_{obs,i} - y_{pred,i})^2}{\sum_{i=1}^{N}(y_{obs,i} - \bar{y}_{obs})^2} \tag{2.1}$$

$$RMSE = \sqrt{\frac{1}{N}\sum_{i=1}^{N}(y_{pred,i} - y_{obs,i})^2} \tag{2.2}$$

$R^2$ was derived from the ordinary least-squares regression of observed values on predicted values. Furthermore, the multiplicative Bias and Mean Absolute Error (MAE) were computed in the base-10 logarithmic domain for all models, as these metrics provide scale-invariant evaluation of relative errors across the wide dynamic range of water quality constituents.

$$Bias = 10^{\frac{1}{N}\sum_{i=1}^{N}(\log_{10}(y_{pred,i}) - \log_{10}(y_{obs,i}))} \tag{2.3}$$

$$MAE = 10^{\frac{1}{N}\sum_{i=1}^{N}|\log_{10}(y_{pred,i}) - \log_{10}(y_{obs,i})|} \tag{2.4}$$

where $y_{pred}$ and $y_{obs}$ represent the model-predicted and in-situ observed values respectively (in mg/m³ for Chlorophyll-a or NTU for turbidity), $\bar{y}_{obs}$ is the mean of the observed values, and N is the number of validation samples.

# Chapter 3 Results

## 3.1 Match-up Dataset Characteristics

The spatiotemporal match-up procedure described in Section 2.2.3 yielded sensor and product specific datasets for model training, alongside shared validation pools for robust inter-sensor comparison. As detailed in Section 2.3.4, validation was restricted to temporally coincident same-date acquisitions from both Sentinel-2 and Landsat-8/9, ensuring environmental comparability across sensors. While the initial spatiotemporal filtering was applied consistently across all configurations, the final number of valid matchups differed significantly between TOA and SR products. Because Sentinel L2A imagery is more susceptible to near-zero reflectance anomalies following atmospheric correction, a greater number of observations had to be excluded from the SR datasets. Consequently, this discrepancy in valid matchups resulted in product-specific validation pool sizes: 73 and 62 for TOA, compared to a reduced 58 and 49 for SR, for Chlorophyll-a and Turbidity respectively. The remaining matchups, which vary in size due to differences in acquisition frequency between the two missions, were allocated exclusively to model training. The final allocation of match-up samples for model development and evaluation during the 2020–2023 period is outlined in Table 3.1. Site-specific sample distributions are provided in Appendix A (Table A.1).

*Table 3.1 Training and validation sample counts across sensor platforms, processing levels, and water quality parameters.*

| Sensor | Product | Chl-a Train | Chl-a Val | Turbidity Train | Turbidity Val |
|---|---|---|---|---|---|
| Sentinel-2 | TOA | 355 | 73 | 308 | 62 |
| Sentinel-2 | SR | 307 | 58 | 263 | 49 |
| Landsat-8/9 | TOA | 106 | 73 | 89 | 62 |
| Landsat-8/9 | SR | 115 | 58 | 101 | 49 |

Sentinel-2 accumulated substantially more training observations than Landsat-8/9 across all configurations (e.g., 355 vs. 106 for TOA Chlorophyll-a), reflecting the higher acquisition frequency of the combined Sentinel-2A/2B constellation compared to the Landsat-8/9 pair (5-day vs. 8-day revisit cycle).

The combined matchup dataset spans a Chlorophyll-a range of 0.07–20.83 mg/m³ (median = 1.06 mg/m³, mean = 1.89 mg/m³) and a Turbidity range of 0.001–21.05 NTU (median = 0.68 NTU, mean = 1.35 NTU). The pronounced positive skewness of both distributions—mean approximately double the median—reflects the dominance of background low-

concentration conditions with occasional high-loading events primarily caused by Po River discharge and seasonal phytoplankton blooms.

### 3.2 Chlorophyll-a Retrieval Results

The validation results for Chlorophyll-a retrieval are summarized in Table 3.2, evaluating the impact of atmospheric processing and spatial resolution. Figure 3.1 shows the corresponding density scatter plots of predicted versus in-situ concentrations for each configuration.

*Table 3.2 Performance metrics for Chlorophyll-a retrieval across sensor platforms, processing levels, and monitoring sites.*

| Sensor | Product | Site | $R^2$ | RMSE (mg/m³) | Bias (mult.) | MAE (mult.) |
|---|---|---|---|---|---|---|
| Sentinel-2 MSI | TOA | Total | 0.68 | 0.82 | 1.07 | 1.47 |
| | | Probe E1 | 0.76 | 0.60 | 1.06 | 1.43 |
| | | Probe S1 | 0.64 | 1.03 | 1.10 | 1.50 |
| | SR | Total | 0.43 | 1.27 | 1.05 | 2.30 |
| | | Probe E1 | 0.77 | 0.84 | 1.21 | 1.57 |
| | | Probe S1 | 0.36 | 1.13 | 1.21 | 1.94 |
| Landsat-8/9 OLI | TOA | Total | 0.58 | 1.51 | 0.99 | 1.54 |
| | | Probe E1 | 0.22 | 1.22 | 1.05 | 1.73 |
| | | Probe S1 | 0.32 | 1.47 | 0.73 | 4.06 |
| | SR | Total | 0.29 | 1.62 | 1.38 | 1.90 |
| | | Probe E1 | 0.59 | 1.72 | 1.31 | 1.63 |
| | | Probe S1 | 0.17 | 1.72 | 0.94 | 4.11 |

*Note: $R^2$ = coefficient of determination; RMSE = Root Mean Square Error (mg/m³); Bias (mult.) = Multiplicative bias computed in $log_{10}$-space (dimensionless factor). Values > 1.0 indicate overestimation; values < 1.0 indicate underestimation. MAE (mult.) = Multiplicative mean absolute error in $log_{10}$-space (dimensionless factor).*

Sentinel-2 MSI demonstrated consistently higher retrieval accuracy than Landsat-8/9 OLI across both processing levels. The Sentinel-2 TOA configuration achieved the best overall performance, with $R^2 = 0.68$ and RMSE = 0.82 mg/m³, while Landsat-8/9 TOA yielded $R^2 = 0.58$ and RMSE = 1.51 mg/m³. This advantage may be observed in the scatter plots (Figure 3.1a vs. 3.1c), where Sentinel-2 TOA shows a tighter distribution around the 1:1 line across the full concentration range, while Landsat-8/9 TOA exhibits greater scatter particularly at concentrations above 2 mg/m³. For SR products, the performance gap widened further:

Sentinel-2 SR achieved $R^2 = 0.43$ and RMSE = 1.27 mg/m³, whereas Landsat-8/9 SR showed the weakest performance of all configurations ($R^2 = 0.29$, RMSE = 1.62 mg/m³), both scatter plots (Figures 3.1b and 3.1d) reveal substantial scatter throughout the entire concentration range and several large overestimation outliers in the low-concentration regime.

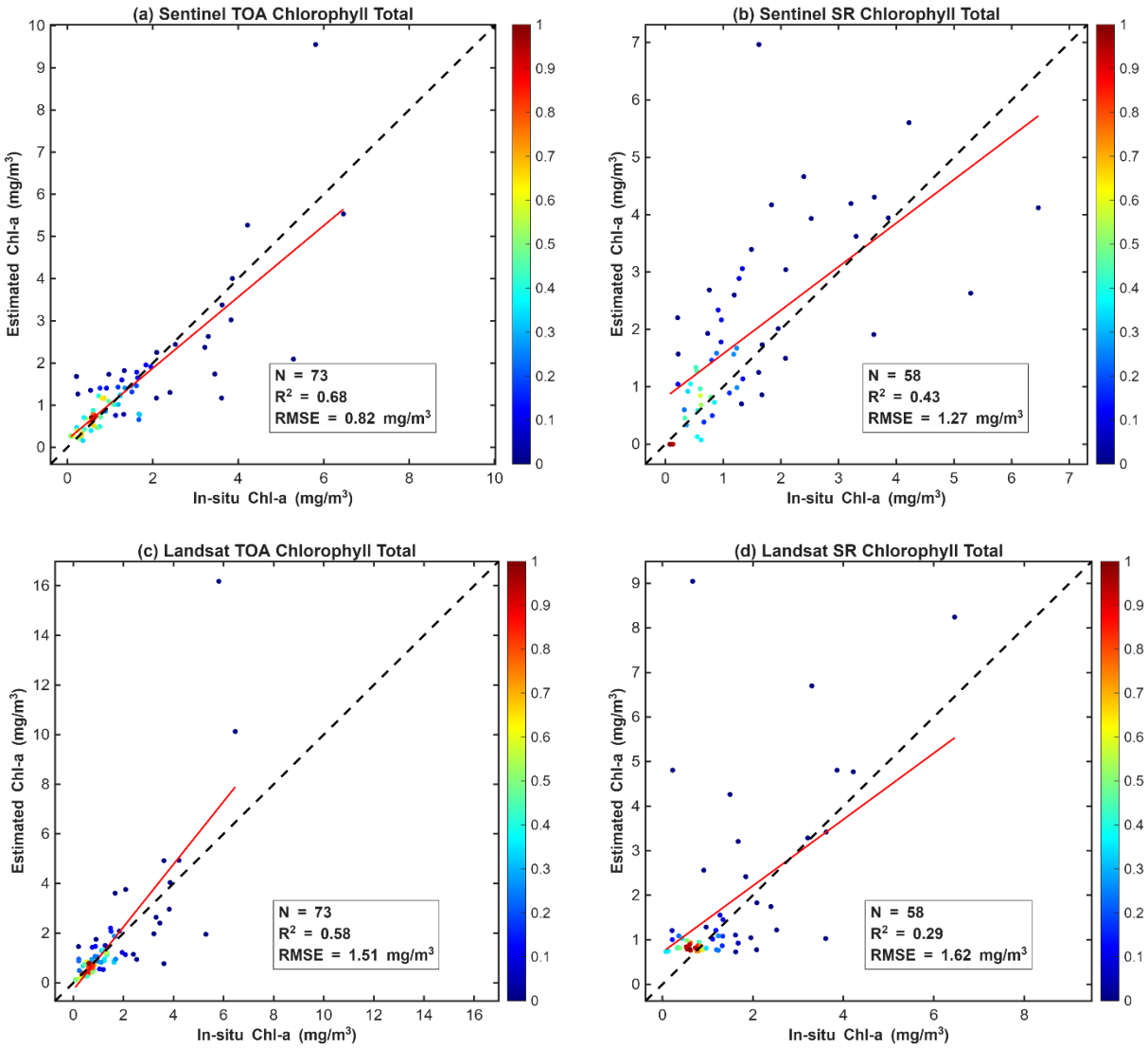


*Figure 3.1 Density scatter plots of Sentinel-2 TOA (a), Sentinel-2 SR (b), Landsat-8/9 TOA (c), and Landsat-8/9 SR (d) neural network estimates versus in-situ Chlorophyll-a measurements. The colour gradient represents the density of data points, with warmer colours indicating higher point concentration. The black dashed line represents the 1:1 relationship; the red solid line shows the linear regression fit. Performance metrics (N, R², RMSE) are displayed in each panel.*

A consistent pattern across both sensors was the superior performance of TOA products over their atmospherically corrected SR counterparts. For Sentinel-2, TOA outperformed SR by 0.25 in $R^2$ (0.68 vs. 0.43) with 35% lower RMSE (0.82 vs. 1.27 mg/m³). For Landsat-8/9, TOA similarly outperformed SR ($R^2$ = 0.58 vs. 0.29; RMSE = 1.51 vs. 1.62 mg/m³). This pattern suggests that the neural network models trained on TOA reflectance can effectively compensate

for atmospheric effects implicitly, potentially avoiding the artefacts introduced by standard atmospheric correction algorithms in the optically complex waters of the study area, as discussed further in Chapter 4.

Site-specific performance showed consistently higher accuracy at Probe E1 than at Probe S1. Using Sentinel-2 TOA, Probe E1 achieved $R^2 = 0.76$ (RMSE = 0.60 mg/m³) compared to $R^2 = 0.64$ (RMSE = 1.03 mg/m³) at Probe S1. Interestingly, while TOA generally outperformed SR across the study, Sentinel-2 SR at Probe E1 proved to be a notable exception, achieving a surprisingly high $R^2 = 0.77$ despite the poor overall performance of the SR configuration. The consistently weaker performance at Probe S1 across most models is likely attributable to the direct influence of Po River plume dynamics at this near-delta location (Section 2.1.2), which introduces high optical variability in suspended sediments and CDOM that presents a greater retrieval challenge.

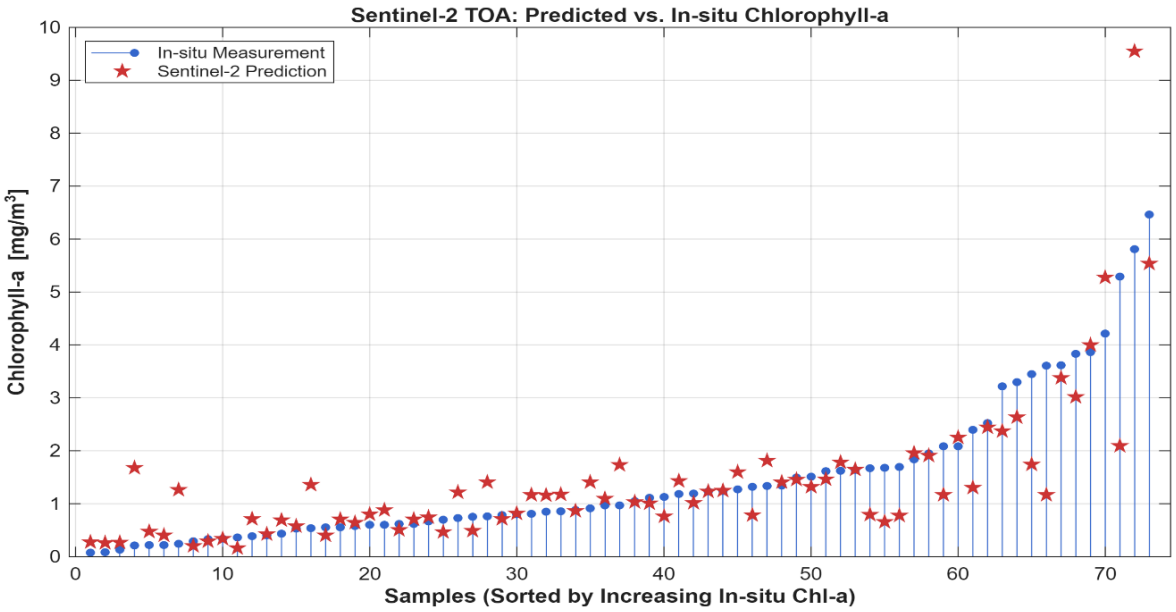


*Figure 3.2 Point-by-point validation of Chlorophyll-a retrievals for Sentinel-2 TOA configuration. Samples are sorted by increasing in-situ concentration along the x-axis. Blue vertical stems represent in-situ measurements. Red star symbols indicate Sentinel-2 TOA neural network predictions.*

Figure 3.2 presents a detailed point-by-point comparison of Chlorophyll-a in situ measurements with predictions based on Sentinel-2 TOA configuration. As the best-performing configuration among those tested, it was selected for this granular residual analysis, with samples sorted by increasing in-situ concentration along the x-axis. The satellite retrievals closely tracked the measured values across the low-to-moderate concentration range (below ~2 mg/m³) that dominates the dataset, with residuals remaining small and evenly distributed. At higher concentrations, corresponding to episodic bloom or river discharge events, the model

shows increased scatter and occasional overestimation, reflecting the reduced representation of extreme conditions in the training dataset.

### 3.3 Turbidity Retrieval Results

The validation results for turbidity retrieval are summarized in Table 3.3, which presents the corresponding density scatter plots of predicted versus in-situ turbidity for each sensor-product configuration.

*Table 3.3 Performance metrics for turbidity retrieval across sensor platforms, processing levels, and monitoring sites.*

| Sensor | Product | Site | $R^2$ | RMSE (NTU) | Bias (mult.) | MAE (mult.) |
|---|---|---|---|---|---|---|
| Sentinel-2 MSI | TOA | Total | 0.75 | 2.26 | 1.08 | 1.74 |
| | | Probe E1 | 0.78 | 2.53 | 0.95 | 1.61 |
| | | Probe S1 | 0.76 | 2.11 | 1.26 | 1.58 |
| | SR | Total | 0.76 | 2.46 | 0.96 | 1.66 |
| | | Probe E1 | 0.66 | 3.32 | 1.04 | 1.54 |
| | | Probe S1 | 0.63 | 2.38 | 0.93 | 1.54 |
| Landsat-8/9 OLI | TOA | Total | 0.51 | 2.87 | 0.91 | 1.84 |
| | | Probe E1 | 0.71 | 3.00 | 0.97 | 1.47 |
| | | Probe S1 | 0.53 | 2.20 | 0.89 | 1.31 |
| | SR | Total | 0.34 | 3.60 | 0.94 | 1.88 |
| | | Probe E1 | 0.66 | 3.96 | 0.84 | 1.75 |
| | | Probe S1 | 0.62 | 2.06 | 0.91 | 1.70 |

*Note: $R^2$ = coefficient of determination; RMSE = Root Mean Square Error (NTU); Bias (mult.) = Multiplicative bias computed in $log_{10}$-space (dimensionless factor). Values > 1.0 indicate overestimation; values < 1.0 indicate underestimation. MAE (mult.) = Multiplicative mean absolute error in $log_{10}$-space (dimensionless factor).*

Sentinel-2 MSI outperformed Landsat-8/9 OLI for turbidity retrieval across both processing levels. Sentinel-2 TOA achieved the highest accuracy ($R^2$ = 0.75, RMSE = 2.26 NTU), while Landsat-8/9 TOA yielded a lower performance ($R^2$ = 0.51, RMSE = 2.87 NTU). Visually, both configurations effectively capture the dominance of low-turbidity background conditions (below 2 NTU); however, as reflected by the drop in $R^2$, the scatter plots (Figure 3.3a vs. 3.3c) indicate that Sentinel-2 TOA maintains a slightly tighter fit along the 1:1 line compared to Landsat-8/9 TOA.

Unlike the Chlorophyll-a results, the TOA versus SR comparison for turbidity showed a more nuanced pattern. For Sentinel-2, TOA and SR performed comparably ($R^2$ = 0.75 vs.

0.76; RMSE = 2.26 vs. 2.46 NTU), suggesting that for turbidity retrieval the neural network model is relatively robust to atmospheric processing level when applied to Sentinel-2. For Landsat-8/9, however, SR performance declined considerably compared to TOA ($R^2$ = 0.34 vs. 0.51; RMSE = 3.60 vs. 2.87 NTU), consistent with the pattern observed for Chlorophyll-a and indicative of greater atmospheric correction artefacts in Landsat SR products over these turbid coastal waters.

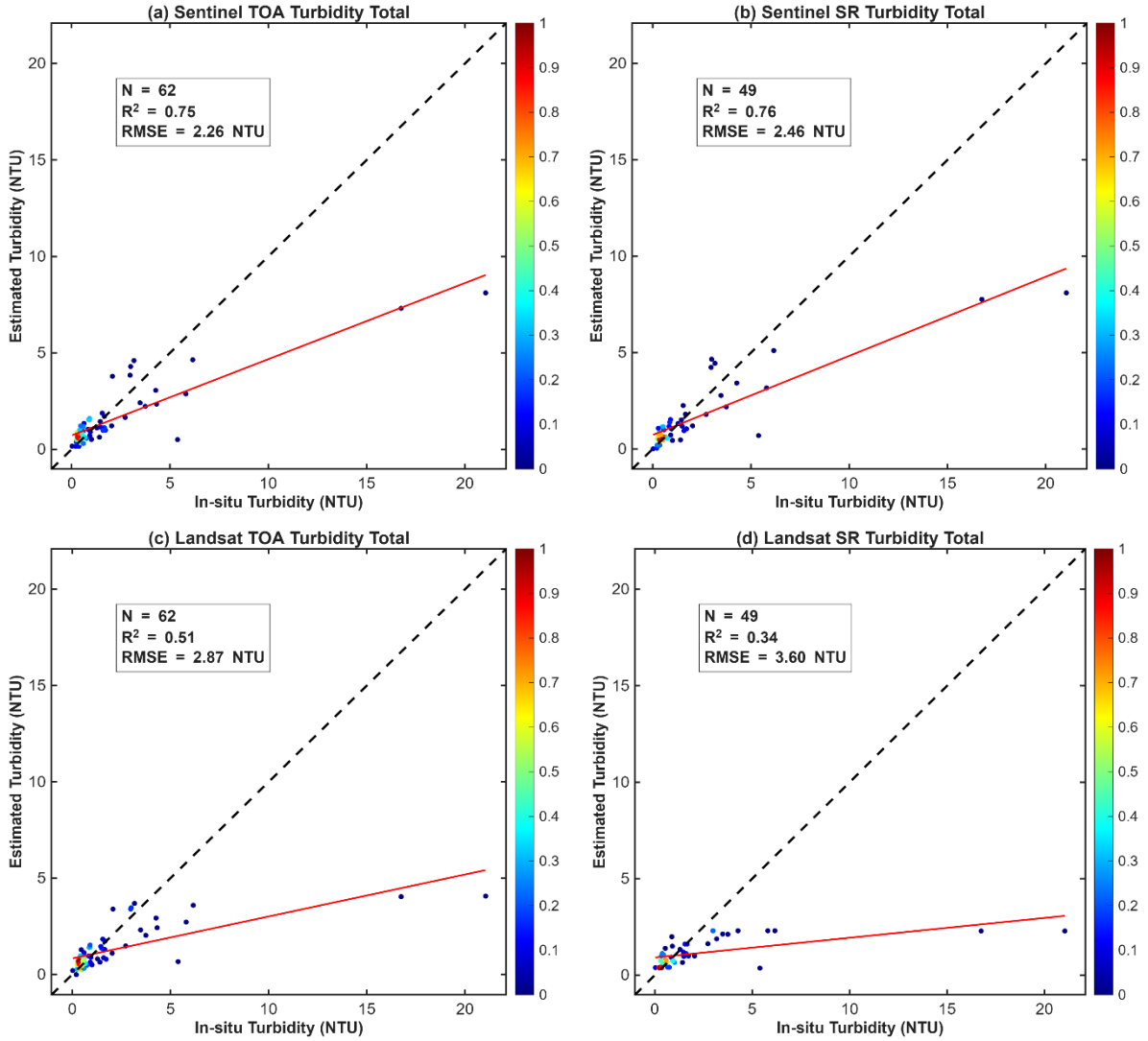


*Figure 3.3 Density scatter plots of Sentinel-2 TOA (a), Sentinel-2 SR (b), Landsat-8/9 TOA (c), and Landsat-8/9 SR (d) neural network estimates versus in-situ Turbidity measurements. The colour gradient represents the density of data points, with warmer colours indicating higher point concentration. The black dashed line represents the 1:1 relationship; the red solid line shows the linear regression fit. Performance metrics (N, R², RMSE) are displayed in each panel.*

Site-specific performance for turbidity was notably more consistent between stations than for Chlorophyll-a. Using Sentinel-2 TOA, Probe E1 achieved $R^2$ = 0.78 (RMSE = 2.53 NTU) and Probe S1 achieved $R^2$ = 0.76 (RMSE = 2.11 NTU), indicating that turbidity retrieval

is comparably robust at both monitoring locations. This contrasts with the Chlorophyll-a results where Probe S1 showed markedly weaker performance and may reflect the fact that turbidity is more directly related to total backscattering—a property that is less susceptible to the complex bio-optical variability introduced by Po River CDOM and phytoplankton co-variation at Probe S1.

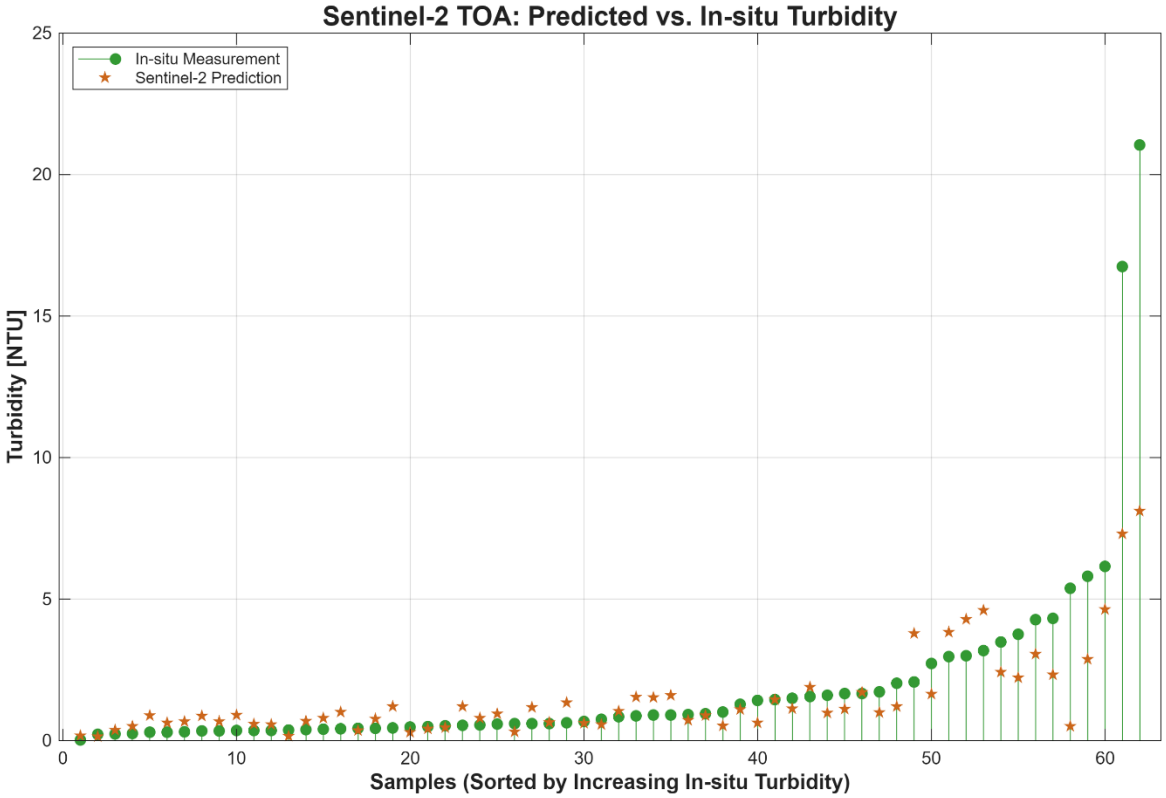


*Figure 3.4 Point-by-point validation of Turbidity retrievals for Sentinel-2 TOA configuration. Samples are sorted by increasing in-situ concentration along the x-axis. Green vertical stems represent in-situ measurements; orange star symbols indicate Sentinel-2 TOA neural network predictions.*

Figure 3.4 presents the point-by-point comparison of turbidity values for Sentinel-2 TOA, with samples sorted by increasing in-situ concentration. The model accurately tracked the predominantly low-turbidity background conditions that characterize the majority of observations. At the two highest turbidity values in the validation set (~17 and ~21 NTU), corresponding to episodic resuspension or river discharge events, the model substantially underestimated the observed concentrations, reflecting the limited representation of extreme turbidity events in the training dataset.

### 3.4 Spatiotemporal Mapping

To demonstrate how the statistical performance differences identified in Sections 3.2 and 3.3 manifest spatially, Chlorophyll-a retrieval was applied across two contrasting dates: 16 August

2023 and 4 November 2023. For 16 August 2023, all four sensor-product configurations were mapped to allow a comprehensive visual assessment of their spatial behaviors, particularly regarding the artefacts introduced by standard atmospheric correction in coastal waters (Figure 3.5). For 4 November 2023, the TOA configurations of both sensors are presented (Figure 3.6), enabling a direct inter-sensor comparison under the most reliable processing level. It should be noted that the neural network models were developed for coastal water quality retrieval; therefore, pixels corresponding to inland water bodies visible within the mapped extent are excluded from interpretation.

### *3.4.1 Spatial Distribution on 16 August 2023*

Figure 3.5 presents the Chlorophyll-a (Chl-a) spatial distribution maps derived from all four configurations for 16 August 2023. All configurations consistently revealed higher Chl-a concentrations across the nearshore zone, with a high-nearshore, low-offshore spatial gradient. This coastal confinement is characteristic of riverine inputs — predominantly from the Po River — interacting with the West Adriatic Coastal Current (WACC), as documented in this region (Vona et al., 2025).

Visually, the overall spatial extent of the Chl-a plume, including its offshore expansion south of the breakwater, was consistent across both sensors. However, the internal distribution of high-concentration zones differed markedly. Sentinel-2 retrievals (Figures 3.5a–b) displayed a smoother and more continuous offshore transition, with only narrow lines of peak concentration immediately adjacent to the coastline and the broader nearshore waters predominantly showing 5–7 mg/m³. In contrast, Landsat-9 retrievals (Figures 3.5c–d) featured a narrower but far more intense nearshore band of peak concentrations, with saturated values frequently reaching 8–10 mg/m³ right against the shore. In addition, the Landsat-9 maps exhibited a more granular spatial texture, rendering the drop from extreme nearshore values to the broader plume more abrupt. These differences in gradient smoothness and texture likely arise from Sentinel-2's finer spatial resolution and its dedicated red-edge spectral bands, which provide greater sensitivity to the gradual offshore dilution of phytoplankton biomass.

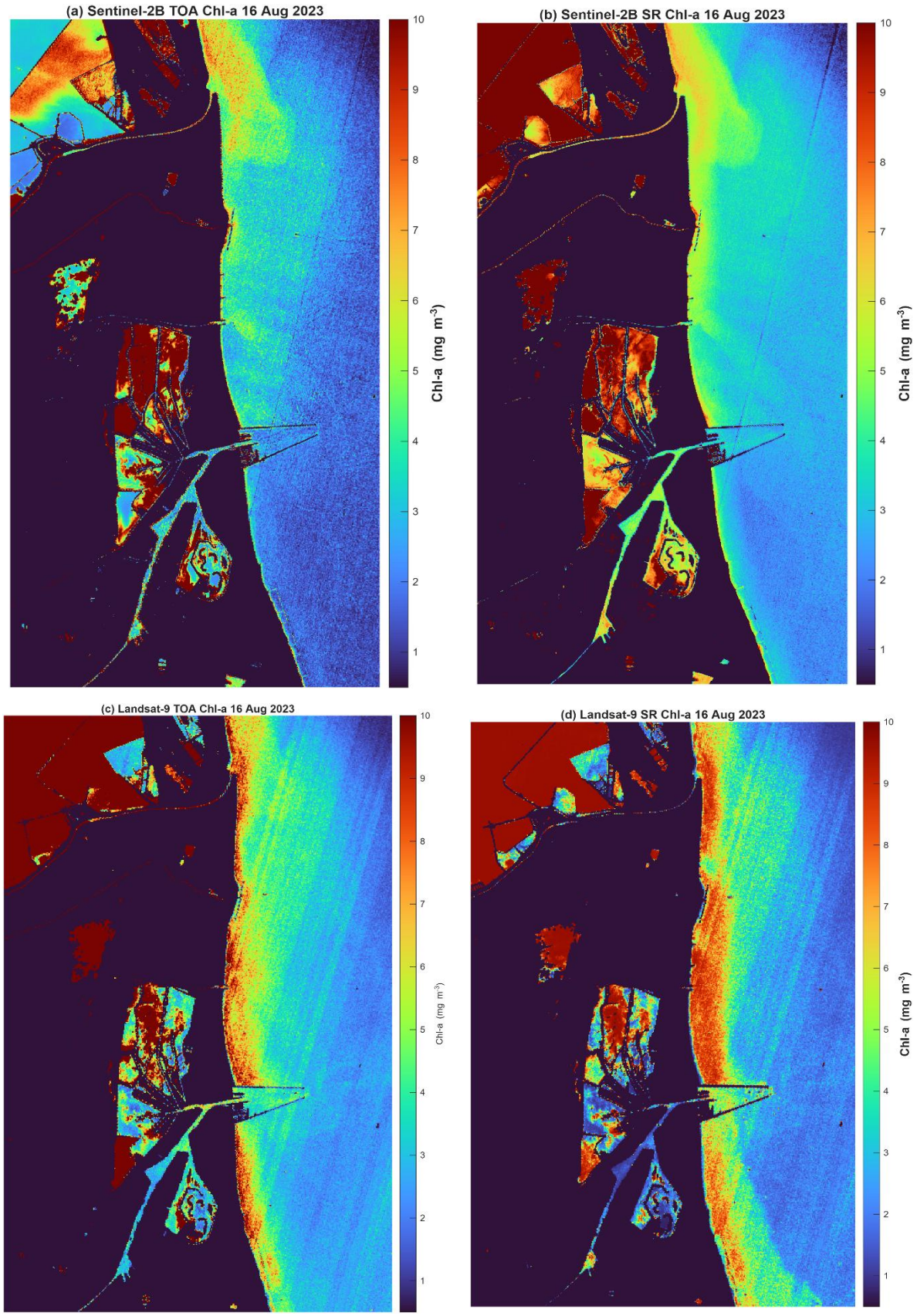


*Figure 3.5 Spatial distribution maps of Chlorophyll-a (Chl-a) concentrations on 16 August 2023. Panels show comparisons between sensors and reflectance products: (a) Sentinel-2B TOA, (b) Sentinel-2B SR, (c) Landsat-9 TOA, and (d) Landsat-9 SR. The mapping of Chl-a concentrations should be interpreted as valid primarily for coastal waters, whereas its applicability to inland waters remains uncertain.*

A clear and consistent difference was also evident between the TOA and SR products for both sensors: SR retrievals generally yielded higher nearshore Chl-a concentrations and a sharper nearshore–offshore contrast than their TOA counterparts. While this pattern may partly result from the removal of atmospheric path radiance, thereby enhancing the water-leaving signal, it is also consistent with the lower validation accuracy of the SR products reported in Section 3.2. This suggests that the standard land-oriented atmospheric correction applied to generate the SR imagery may introduce a positive bias in nearshore Chl-a retrievals over these optically complex coastal waters.

*3.4.2 Spatial Distribution on 4 November 2023*

As illustrated in Figure 3.6(a), the Sentinel-2B TOA Chlorophyll-a (Chl-a) map for 4 November 2023 shows very low background concentrations across most of the open coastal waters. These regions are dominated by deep blue tone, corresponding to values predominantly ≤ 2 mg/m$^3$. The most prominent high-concentration patch occurs in the northern part of the imaged coastal zone. It exhibits a distinct plume-like structure with a saturated red core (peak values reaching 8–10 mg/m$^3$). This core is sequentially surrounded by rings of yellow (≈ 5–7 mg/m$^3$) and light green to cyan (≈ 3–5 mg/m$^3$) waters, before rapidly transitioning into the prevailing deep blue background. This physical feature extends only a short distance offshore and fades abruptly into the low-concentration field. Additionally, a smaller, much weaker anomaly is visible along the central coastline (near the breakwater). It appears as a narrow cyan-to-light-green protrusion (≈ 2–4 mg/m$^3$) that dissipates quickly without forming a strong intensity gradient or an extended filament.

The contemporaneous Landsat-9 TOA retrieval (Figure 3.6b) reveals notable differences in both background levels and the spatial representation of nearshore features. Across the open coastal waters, the Landsat-9 map exhibits a higher and more spatially heterogeneous background, with offshore regions dominated by light blue to cyan hues generally ranging between 2 and 4 mg/m³, in contrast to the uniform deep blue background observed in the Sentinel-2 retrieval. The prominent northern plume remains discernible, with a saturated core approaching or exceeding 10 mg/m³ and a notably larger areal extent of elevated concentrations compared to the equivalent feature in the Sentinel-2 retrieval. Along the central coastline, Landsat-9 produces a highly localized but intensely elevated retrieval, with a saturated red core that has no counterpart of comparable magnitude in the Sentinel-2 map.

Overall, the Landsat-9 retrievals exhibit a coarser spatial texture and elevated background concentrations relative to Sentinel-2.

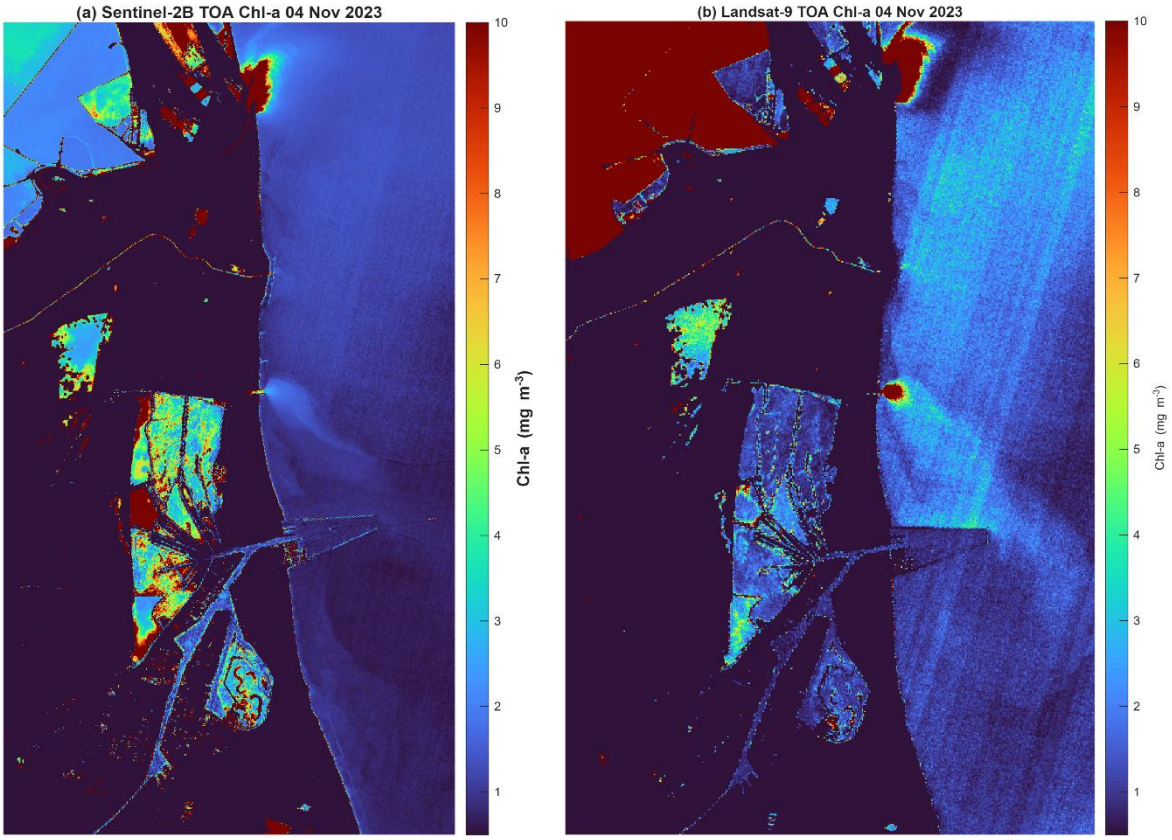


*Figure 3.6 Spatial distribution of Chlorophyll-a (Chl-a) concentration derived from (a) Sentinel-2B TOA and (b) Landsat-9 TOA reflectance on 4 November 2023 The mapping of Chl-a concentrations should be interpreted as valid primarily for coastal waters, whereas its applicability to inland waters remains uncertain*

Despite the inter-sensor differences noted above, both retrievals concur in depicting a coastal sea with high spatial uniformity in the background, with no evidence of the broad nearshore-to-offshore gradients or widespread elevated bands observed in the August data. Strong concentration contrasts are entirely confined to these isolated river mouth patches, where sharp local gradients occur over short distances before merging into the homogeneous, low Chl-a open water.

# Chapter 4 Discussion

## 4.1 Effect of Atmospheric Correction on Model Performance

A primary finding of this study is the systematic superiority — or at least comparability — of neural network models trained on TOA reflectance over SR. While the magnitude of this advantage varied, it was particularly stark for Chlorophyll-a retrieval across both sensors, where standard atmospheric correction introduced substantial performance degradation (Table 3.2). For Turbidity, the TOA advantage was more nuanced for Sentinel-2 but remained clearly evident for Landsat-8/9 (Table 3.3). Collectively, these trends demonstrate that the detrimental effect of standard atmospheric correction in these coastal waters is highly dependent on both the target biogeochemical parameter and the sensor's configuration.

These results are consistent with the well-documented limitations of standard atmospheric correction algorithms in optically complex coastal waters. As outlined in Section 1.2, most standard processors rely on the assumption of near-zero water-leaving radiance in the near-infrared (NIR) band. However, this assumption is frequently violated in highly turbid coastal waters, where elevated concentrations of suspended particulate matter induce significant backscattering in the NIR region (Vanhellemont and Ruddick, 2021; Zhang et al., 2023). Consequently, processors such as Sen2Cor often perform poorly in sediment-laden coastal environments (Bui et al., 2022), including the Emilia-Romagna coast, which is strongly influenced by the highly turbid Po River plume (Braga et al., 2017). Under such conditions, imperfect aerosol characterization introduces systematic biases in the retrieved surface reflectance, thereby corrupting the spectral signal required for accurate chlorophyll-a inversion. This interpretation is further supported by the substantially smaller number of valid surface reflectance (SR) matchups retained after quality screening in this study (307 vs. 355 for Sentinel-2 TOA Chlorophyll-a; Table 3.1). A considerable proportion of the atmospherically corrected spectra exhibited near-zero or physically implausible reflectance values and had to be discarded, which reduced both the training sample size and its representativeness.

Conversely, the superior performance of TOA trained models suggests that the neural network is capable of implicitly learning and compensating for the atmospheric signal embedded in TOA reflectance, provided that sufficient training data spanning the range of atmospheric variability are available. This finding is consistent with recent studies demonstrating that data-driven models operating directly on TOA or minimally corrected reflectance can successfully bypass the limitations of explicit atmospheric correction and

achieve competitive or superior performance compared to SR-based approaches in turbid coastal waters (Hadjal et al., 2022). This is plausible given that the training matchups span four years (2020–2023) and thus capture a broad range of atmospheric states over the study area. It also echoes the motivation articulated in Section 1.2: rather than propagating atmospheric correction errors into the input features, the neural network implicitly accounts for the atmospheric signal as part of the learned end-to-end reflectance-to-concentration mapping.

It should be acknowledged, however, that this implicit atmospheric compensation is not equivalent to a physically rigorous retrieval. The TOA model's learned mapping is specific to the atmospheric conditions present in the training dataset; its ability to generalize to scenes with substantially different aerosol optical depth or composition — for instance, during Saharan dust intrusion events (Barnaba and Gobbi, 2004) — cannot be guaranteed without further evaluation. Nonetheless, for routine monitoring within a well-characterized regional environment such as the Northern Adriatic, the empirical evidence from this study supports the preferential use of TOA reflectance as model input, particularly given the documented limitations of operational atmospheric correction in nearshore turbid waters.

### 4.2 Inter-sensor Performance: Sentinel-2 versus Landsat-8/9

Across both target variables and both processing levels, Sentinel-2 consistently outperformed Landsat-8/9. For Chlorophyll-a retrieval under TOA conditions — where both sensors achieved their respective best performance — Sentinel-2 attained an $R^2$ of 0.68 and RMSE of 0.82 mg/m³, compared to $R^2 = 0.58$ and RMSE = 1.51 mg/m³ for Landsat-8/9 (Table 3.2). The performance disparity was more pronounced at the site level: at Probe S1, the Landsat-8/9 TOA model yielded an $R^2$ of only 0.32 with a multiplicative MAE of 4.06, indicating substantial scatter that likely reflects the sensor's reduced capacity to resolve the extreme optical variability near the Po River mouth (Table 3.2). For Turbidity, the inter-sensor gap was comparatively smaller, suggesting that the spectral advantage of Sentinel-2 is more consequential for the optically complex Chlorophyll-a signal than for turbidity, which is more directly linked to broadband backscattering (Table 3.3).

The superior performance of Sentinel-2 can be attributed to two complementary factors: spectral configuration and spatial resolution. Sentinel-2 MSI includes three Red-Edge bands (B5 at 705 nm, B6 at 740 nm, B7 at 783 nm) that are absent in the Landsat-8/9 OLI. These bands straddle the chlorophyll absorption feature at 670 nm and the onset of high phytoplankton reflectance beyond 700 nm, a spectral region that has been shown to carry strong diagnostic

information for Chlorophyll-a in turbid and eutrophic waters where blue-band signals are heavily contaminated by CDOM absorption (Gitelson et al., 2008; Mishra and Mishra, 2012). The inclusion of these bands in the input feature space provides the neural network with additional discriminatory power that the seven-band Landsat OLI configuration cannot replicate.

Spatial resolution also likely contributes to the observed performance gap. Although the Sentinel-2 Coastal Aerosol band (B1) has a native resolution of 60 m, the primary bio-optical diagnostic bands — including the visible, red-edge, and near-infrared channels — operate at finer native resolutions of 10–20 m. When harmonized to a 20 m grid, these bands retain greater spatial detail than the 30 m Landsat OLI configuration. This enhanced spatial granularity reduces the prevalence of mixed pixels and enables improved detection of fine-scale bio-optical gradients near the shoreline (Pahlevan et al., 2017; Vanhellemont and Ruddick, 2018). The effect is particularly relevant at Probe E1, located approximately 4 nautical miles offshore, where strong nearshore gradients are expected.

Finally, the substantially larger training dataset available for Sentinel-2 (355 vs. 106 samples for TOA Chlorophyll-a; Table 3.1) is a confounding factor that must be acknowledged. The higher acquisition frequency of the Sentinel-2A/2B constellation means that the model had access to approximately three times as many training examples, which may itself contribute to better generalization. It is therefore not possible to fully disentangle the contribution of spectral configuration from that of training sample size in explaining the observed performance gap. A controlled experiment using equal sample sizes would be required to isolate these effects, which falls beyond the scope of this study.

### 4.3 Site-Specific Performance and the Role of Optical Complexity

A consistent pattern across all sensor and product configurations is the systematic divergence in retrieval performance between the two monitoring stations. For Chlorophyll-a, Probe E1 generally outperformed Probe S1 — most clearly under SR conditions, where E1 and S1 yielded $R^2 = 0.77$ and $R^2 = 0.36$ respectively for Sentinel-2, while the Landsat-8/9 multiplicative MAE at S1 reached 4.06–4.11 across both processing levels, two to three times higher than at E1 (Table 3.2). For Turbidity, inter-site differences were comparatively smaller across most configurations (Table 3.3), a contrast that is consistent with the underlying optical mechanisms: unlike turbidity, which is governed by robust broadband backscattering from suspended solids, Chlorophyll-a retrieval depends on narrow absorption features that are readily masked by the

intense, co-varying absorption of riverine CDOM and non-algal particles near the Po River mouth (Berthon and Zibordi, 2004; Gitelson et al., 2008). This distinction suggests that the performance penalty at S1 is not a general consequence of poor signal quality but rather reflects the specific optical complexity that confounds Chlorophyll-a retrievals in highly turbid, CDOM-rich waters.

The elevated difficulty at Probe S1 is consistent with its geographic setting. Located approximately 4 nautical miles south of the Po di Goro mouth within the Po River Delta system, Probe S1 is subject to episodic, high-magnitude discharge events that introduce large and rapid fluctuations in suspended particulate matter, CDOM, and nutrients (Section 2.1.2). These inputs create highly variable and partially decoupled optical conditions, where the relationship between water-leaving reflectance and Chlorophyll-a concentration is modulated by co-varying CDOM and sediment loads (Matsushita et al., 2012; Kyryliuk and Kratzer, 2019) in ways that are difficult for a fixed-architecture neural network to resolve from spectral information alone. As noted by Berthon and Zibordi (2004) and Manzo et al. (2018), the Northern Adriatic coastal zone — and particularly the area proximal to the Po River plume — represents one of the most optically challenging environments for satellite-based water quality retrieval, precisely because the standard bio-optical assumptions that underpin spectral inversion break down under high CDOM and sediment loading.

An additional contributing factor is the statistical composition of the training dataset. The pronounced positive skewness of the Chlorophyll-a and Turbidity distributions (Section 3.1) implies that high-concentration events, which are disproportionately associated with Po River discharge and more likely to occur at Probe S1, are underrepresented in the training data relative to background low-concentration conditions. This imbalance fundamentally limits the model's ability to generalize to the upper tail of the concentration range at Probe S1, a constraint consistent with the general principle that empirical machine learning models are inherently bounded by the variable ranges represented in their training data (Sagan et al., 2020). The resulting poor generalization at high concentrations is reflected in the elevated scatter and MAE values observed at this site. Future work could address this through targeted data augmentation strategies or by weighing training samples according to their representativeness of the full concentration range.

## 4.4 Spatiotemporal Distribution of Chlorophyll-a: Seasonal Dynamics and Spatial Artefacts

While the point-based statistical metrics discussed in previous sections establish the quantitative accuracy of the retrieval models, the overarching value of satellite remote sensing lies in its synoptic capacity to capture large-scale spatial gradients and dynamic physical processes. The application of the trained neural networks to full satellite scenes (Section 3.4) serves as a critical test of model robustness, verifying whether the algorithms can reproduce physically realistic hydrodynamic structures across varying seasonal conditions.

The Chlorophyll-a spatial distribution maps for 16 August 2023 (Figure 3.5) clearly illustrate the summer dynamics of the coastal zone. All sensor configurations successfully captured a pronounced nearshore-to-offshore gradient, driven by riverine inputs — primarily from the Po River — interacting with the West Adriatic Coastal Current (WACC) (Vona et al., 2025). However, the qualitative differences between the satellite products provide compelling visual corroboration of the quantitative results presented in Chapter 3 and further analyzed in Sections 4.1 and 4.2.

Notably, Sentinel-2 retrievals demonstrated a smoother, more continuous offshore transition of the phytoplankton plume, accurately reflecting the gradual dilution of biomass. In contrast, Landsat-9 maps exhibited a granular spatial texture with abrupt concentration drops and saturated nearshore bands. This visual disparity highlights the tangible benefits of Sentinel-2's finer spatial resolution and its dedicated red-edge bands, which collectively offer superior sensitivity to subtle bio-optical gradients. Furthermore, the systematic differences between TOA and SR configurations observed in the maps — where SR products yielded a sharper contrast and notably higher nearshore concentrations — reinforce the conclusion from Section 4.1. This spatial pattern provides evidence that standard land-oriented atmospheric corrections (such as Sen2Cor and LaSRC) produce substantial Rrs retrieval errors over optically complex, highly turbid nearshore waters (Ilori et al., 2019; Warren et al., 2019), potentially compromising Chlorophyll-a estimates where CDOM, sediment loads, and coastal adjacency effects peak.

The TOA retrievals for 4 November 2023 (Figure 3.6) further demonstrate the models' generalization capabilities under contrasting environmental conditions. Despite the inter-sensor differences in background levels and spatial texture documented in Section 3.4.2, both Sentinel-2B and Landsat-9 agree in the absence of the widespread nearshore-to-offshore gradients characteristic of the August scene, with elevated concentrations confined to localized river

mouth features rather than forming broad coastal bands. The model effectively isolates distinct, localized plume structures — such as the saturated core in the northern sector and the minor anomaly near the breakwater — without propagating noise into the homogeneous offshore waters. This ability to accurately resolve both expansive, intense summer plumes and isolated autumn anomalies against a prevailing low-background field suggests that the neural network exhibits some capacity to generalize across diverse bio-optical states, though further validation across additional seasonal scenes would strengthen this conclusion.

### 4.5 Limitations and Directions for Future Research

Several limitations of the present study should be acknowledged when interpreting its findings. First, the in-situ dataset is derived exclusively from two fixed moored sensors, Probe S1 and Probe E1, rather than from spatially distributed field campaigns. While this configuration provides a continuous four-year time series that is well-suited for temporal matchup, it fundamentally constrains the spatial representativeness of the training data. The neural network models are calibrated to the bio-optical conditions characteristic of these two specific locations; their capacity to generalize to other parts of the Romagna coastal zone — including the nearshore areas depicted in the spatiotemporal maps of Section 3.4 — cannot be verified without independent in-situ measurements distributed across the mapping domain. The spatial maps presented in this study should therefore be interpreted as indicative of broad-scale distribution patterns rather than as spatially validated retrievals.

Second, as discussed in Section 4.3, the pronounced positive skewness of both the Chlorophyll-a and Turbidity distributions (Section 3.1) introduces a structural imbalance in the training dataset, where extreme high-concentration events are underrepresented relative to background conditions. While this imbalance fundamentally contributes to the elevated errors observed at Probe S1, it more broadly limits the models' reliability during episodic Po River discharge events—precisely the critical periods most relevant for environmental monitoring and early warning applications. Addressing this limitation would require moving beyond fixed-interval monitoring towards event-driven field campaigns that specifically target high-discharge episodes. Complementary data augmentation strategies, such as synthetic oversampling of extreme values, could further improve model performance during these critical periods.

Third, the temporal transferability of the trained models has not been evaluated. All models were trained and validated on data from the 2020–2023 period, and their performance

under different inter-annual climate conditions — for instance, drought years with anomalously low Po River discharge, or years with unusually intense algal bloom events — remains unknown. Long-term monitoring programs that extend the temporal coverage of the in-situ dataset would be necessary to assess and improve the robustness of the models across a wider range of environmental states.

Finally, while the multi-sensor approach combining Sentinel-2 and Landsat-8/9 effectively enhances temporal resolution, the inter-sensor consistency demonstrated in this study is contingent on the stable radiometric performance of both missions. The analysis was not extended to include Sentinel-2C, which was successfully launched in September 2024 (ESA, 2024), or potential future Landsat missions. The spectral and radiometric characteristics of these new platforms may require a re-evaluation and recalibration of the trained models before operational deployment.

# Chapter 5 Conclusions

This study investigated the retrieval of Chlorophyll-a concentration and Turbidity in the optically complex coastal waters of the Emilia-Romagna region, utilizing neural network models applied to multi-sensor satellite observations from Sentinel-2 MSI and Landsat-8/9 OLI. Through the application of a Bayesian hyperparameter optimization framework, robust Multilayer Perceptron (MLP) architectures were successfully identified across all sensor-product configurations without manual intervention. The best-performing model, based on Sentinel-2 TOA reflectance, achieved an $R^2$ of 0.68 and RMSE of 0.82 mg/m$^3$ for Chlorophyll-a, and an $R^2$ of 0.75 and RMSE of 2.26 NTU for Turbidity. This demonstrates that optimally tuned neural networks can successfully capture the complex, non-linear relationships between satellite reflectance and water quality parameters in a highly dynamic Case-2 coastal environment. Furthermore, the application of a $\log_{10}$ transformation to the TOA-based Chlorophyll-a models significantly improved convergence and reduced bias, effectively accommodating the wide dynamic range of the target variable.

Building upon these validated models, the inter-sensor comparison and evaluation of atmospheric correction effects yielded two clear and consistent findings. First, Sentinel-2 systematically outperformed Landsat-8/9 across both target variables and processing levels, an advantage directly attributable to its dedicated Red-Edge spectral bands, finer spatial resolution, and the larger training sample size afforded by its higher revisit frequency. Second, and more critically, models trained on TOA reflectance consistently outperformed their atmospherically corrected SR counterparts. This demonstrates that standard, land-oriented atmospheric correction processors introduce systematic biases in the optically turbid nearshore environment of the Romagna coast. Instead, neural networks trained directly on TOA reflectance can implicitly compensate for atmospheric effects, yielding more reliable retrievals than those dependent on imperfectly corrected surface data.

Beyond point-based statistical validation, the generation of high-resolution spatiotemporal distribution maps successfully captured the dynamic seasonal regimes of the Northern Adriatic. The Chlorophyll-a maps for 16 August and 4 November 2023 illustrated two contrasting environmental states: a broad nearshore high-concentration band in August, consistent with summer thermal stratification and accumulated nutrient loading from the Po River; and uniformly low open-water concentrations in November, punctuated by distinct, localized river mouth plumes driven by episodic autumnal discharges. Together, these maps

illustrate the operational potential of this multi-sensor neural network approach for routine monitoring of coastal water quality dynamics.

Ultimately, the core contribution of this study lies in challenging the conventional reliance on standard surface reflectance products for coastal monitoring. The results provide compelling evidence that in optically complex, highly turbid environments — where the reliability of standard atmospheric correction is severely compromised — utilizing TOA reflectance as the direct input for neural network retrieval offers a more robust and methodologically sound alternative.

To transition this framework towards a fully operational monitoring system, future research should address current data limitations through three key avenues: (1) conducting spatially distributed field campaigns to validate and improve the models' spatial transferability; (2) incorporating event-driven sampling strategies to better capture extreme plume concentrations and reduce statistical imbalances; and (3) extending this multi-sensor approach to encompass newer platforms (e.g., Sentinel-2C) and longer time series. These steps will be crucial for decoding inter-annual climate variability and long-term ecological trends in the Northern Adriatic Sea.

## Acknowledgements

I would like to express my sincere gratitude to my supervisors, Professor Sonia Silvestri and Dr. Milad Niroumand-Jadidi, for their invaluable guidance and unwavering support throughout this journey.

Professor Sonia Silvestri guided me from the very beginning in defining the research direction and provided essential resources that shaped the foundation of this thesis. What I am most grateful for, however, goes beyond academic supervision. During the periods when I struggled to move forward and lost contact, she reached out and brought me back on track — not with frustration or reproach, but with patience and genuine care. Through every delay and setback, her support never wavered. I could not have completed this work without that kindness.

Dr. Milad Niroumand-Jadidi provided thorough methodological guidance and detailed advice on academic writing, particularly in the application of neural networks to water quality retrieval from remote sensing imagery. There was always encouragement and understanding rather than pressure. That generosity made a real difference in seeing this through to the end.

I am also grateful to my colleagues in the WACOMA program for their companionship, understanding, and encouragement throughout this journey. Together we travelled to Sardinia, Venice, Cesenatico, and many other places, shared meals, and studied side by side in the library. I still remember my birthday in Chioggia during our field trip to the Venice Lagoon — together with Professor Silvestri — and all the warmth that came with it. These are memories I will always carry with me.

The data underlying this research were made possible through the generosity of several institutions. I would like to thank Francesco Riminucci of the Institute of Marine Sciences of the National Research Council (CNR-ISMAR), Bologna, Italy, for providing the in-situ probe data, as well as Copernicus and NASA for making their satellite data openly available. This work was supported by the project "Adriatic coastal areas science-based solutions for climate adaptation" (AdriaClimPlus-ITHR0200333), funded by the Interreg Italy-Croatia cooperation program.

Finally, to my family, friends, and everyone who supported me along the way — thank you for your comfort, patience, and for believing in me, even when I found it difficult to do so myself.

In preparing this thesis, generative AI tools were used to assist with code generation and drafting of text based on the author's own research, data, and results. All content has been reviewed and validated by the author and supervisors. The author takes full responsibility for the accuracy and integrity of the work presented.

## References


1. Adjovu, G.E., Stephen, H., James, D., Ahmad, S., 2023. Overview of the Application of Remote Sensing in Effective Monitoring of Water Quality Parameters. Remote Sensing 15, 1938. https://doi.org/10.3390/rs15071938
2. Bailey, S.W., Werdell, P.J., 2006. A multi-sensor approach for the on-orbit validation of ocean color satellite data products. Remote Sensing of Environment 102, 12–23. https://doi.org/10.1016/j.rse.2006.01.015
3. Barnaba, F., Gobbi, G.P., 2004. Aerosol seasonal variability over the Mediterranean region and relative impact of maritime, continental and Saharan dust particles over the basin from MODIS data in the year 2001. Atmospheric Chemistry and Physics 4, 2367–2391. https://doi.org/10.5194/acp-4-2367-2004
4. Berger, W.H., Smetacek, V.S. and Wefer, G. (1989) 'Ocean productivity and paleoproductivity-an overview' , in Berger, W.H., Smetacek, V.S. and Wefer, G. (eds.) Productivity of the Ocean: Present and Past. John Wiley & Sons Limited , pp. 1-34.
5. Berthon, J.-F., Zibordi, G., 2004. Bio-optical relationships for the northern Adriatic Sea. International Journal of Remote Sensing 25, 1527–1532. https://doi.org/10.1080/01431160310001592544
6. Boldrin, A., Langone, L., Miserocchi, S., Turchetto, M. and Acri, F., 2005. Po River plume on the Adriatic continental shelf: Dispersion and sedimentation of dissolved and suspended matter during different river discharge rates. Marine Geology, 222–223, pp.135–158. https://doi.org/10.1016/j.margeo.2005.06.010
7. Braga, F., Zaggia, L., Bellafiore, D., Bresciani, M., Giardino, C., Lorenzetti, G., Maicu, F., Manzo, C., Riminucci, F., Ravaioli, M. and Brando, V.E., 2017. Mapping turbidity patterns in the Po river prodelta using multi-temporal Landsat 8 imagery. Estuarine, Coastal and Shelf Science, 198, pp.555–567. https://doi.org/10.1016/j.ecss.2016.11.003
8. Brando, V.E., Braga, F., Zaggia, L., Giardino, C., Bresciani, M., Matta, E., Bellafiore, D., Ferrarin, C., Maicu, F., Benetazzo, A., Bonaldo, D., Falcieri, F.M., Coluccelli, A., Russo, A., Carniel, S., 2015. High-resolution satellite turbidity and sea surface temperature observations of river plume interactions during a significant flood event. Ocean Sci. 11, 909–920. https://doi.org/10.5194/os-11-909-2015
9. Breitburg, D., Levin, L.A., Oschlies, A., Grégoire, M., Chavez, F.P., Conley, D.J., Garçon, V., Gilbert, D., Gutiérrez, D., Isensee, K., Jacinto, G.S., Limburg, K.E., Montes, I., Naqvi, S.W.A., Pitcher, G.C., Rabalais, N.N., Roman, M.R., Rose, K.A., Seibel, B.A., Telszewski, M., Yasuhara, M., Zhang, J., 2018. Declining oxygen in the global ocean and coastal waters. Science 359, eaam7240.https://doi.org/10.1126/science.aam7240
10. Brockmann, C., Doerffer, R., Peters, M., Stelzer, K., Embacher, S. and Ruescas, A. (2016) 'Evolution of the C2RCC neural network for Sentinel 2 and 3 for the retrieval of ocean colour products in normal and extreme optically complex waters', Proceedings of the ESA Living Planet Symposium, Prague, 9–13 May 2016.

11. Bui, Q.-T., Jamet, C., Vantrepotte, V., Mériaux, X., Cauvin, A., Mograne, M.A., 2022. Evaluation of Sentinel-2/MSI Atmospheric Correction Algorithms over Two Contrasted French Coastal Waters. Remote Sensing 14, 1099. https://doi.org/10.3390/rs14051099
12. Cosby, A.G., Lebakula, V., Smith, C.N., Wanik, D.W., Bergene, K., Rose, A.N., Swanson, D., Bloom, D.E., 2024. Accelerating growth of human coastal populations at the global and continent levels: 2000–2018. Sci Rep 14, 22489. https://doi.org/10.1038/s41598-024-73287-x
13. Creel, L. (2003) Ripple Effects: Population and Coastal Regions. Washington, DC: Population Reference Bureau.
14. Degobbis, D. and Gilmartin, M., 1990. Nitrogen, phosphorus, and biogenic silicon budgets for the northern Adriatic Sea. Oceanologica Acta, 13, pp.31–45.
15. Drusch, M., Del Bello, U., Carlier, S., Colin, O., Fernandez, V., Gascon, F., Hoersch, B., Isola, C., Laberinti, P., Martimort, P., Meygret, A., Spoto, F., Sy, O., Marchese, F., Bargellini, P., 2012. Sentinel-2: ESA's Optical High-Resolution Mission for GMES Operational Services. Remote Sensing of Environment 120, 25–36. https://doi.org/10.1016/j.rse.2011.11.026
16. ESA, 2024. Sentinel-2C joins the Copernicus family in orbit [Press release]. European Space Agency. Available at: https://www.esa.int/Applications/Observing_the_Earth/Copernicus/Sentinel-2/Sentinel-2C_joins_the_Copernicus_family_in_orbit
17. European Space Agency (2024). MSI L2A DQR March 2024. OMPC.CS.DQR.002.02-2024, Version 71.0. European Space Agency.
18. Falcieri, F.M., Benetazzo, A., Sclavo, M., Russo, A. and Carniel, S., 2014. Po River plume pattern variability investigated from model data. Continental Shelf Research, 87, pp.84–95. https://doi.org/10.1016/j.csr.2013.11.001
19. Gege, P., 2014. WASI-2D: A software tool for regionally optimized analysis of imaging spectrometer data from deep and shallow waters. Computers & Geosciences 62, 208–215. https://doi.org/10.1016/j.cageo.2013.07.022
20. Gitelson, A.A., Dall'Olmo, G., Moses, W., Rundquist, D.C., Barrow, T., Fisher, T.R., Gurlin, D., Holz, J., 2008. A simple semi-analytical model for remote estimation of chlorophyll-a in turbid waters: Validation. Remote Sensing of Environment 112, 3582–3593. https://doi.org/10.1016/j.rse.2008.04.015
21. Hadjal, M., Medina-Lopez, E., Ren, J., Gallego, A., McKee, D., 2022. An Artificial Neural Network Algorithm to Retrieve Chlorophyll a for Northwest European Shelf Seas from Top of Atmosphere Ocean Colour Reflectance. Remote Sensing 14, 3353. https://doi.org/10.3390/rs14143353
22. Hoegh-Guldberg, O., Beal, D., Chaudhry, T., Elhaj, H., Abdullat, A., Etessy, P. and Smits, M. (2015) Reviving the Ocean Economy: The Case for Action – 2015. Gland, Switzerland: WWF International, 60 pp.
23. Ilori, C.O., Pahlevan, N., Knudby, A., 2019. Analyzing Performances of Different Atmospheric Correction Techniques for Landsat 8: Application for Coastal Remote Sensing. Remote Sensing 11, 469. https://doi.org/10.3390/rs11040469

24. Kwong, I.H.Y., Wong, F.K.K., Fung, T., 2022. Automatic Mapping and Monitoring of Marine Water Quality Parameters in Hong Kong Using Sentinel-2 Image Time-Series and Google Earth Engine Cloud Computing. Front. Mar. Sci. 9, 871470. https://doi.org/10.3389/fmars.2022.871470
25. Kyryliuk, D., Kratzer, S., 2019. Summer Distribution of Total Suspended Matter Across the Baltic Sea. Front. Mar. Sci. 5, 504. https://doi.org/10.3389/fmars.2018.00504
26. Legleiter, C.J., Roberts, D.A., Lawrence, R.L., 2009. Spectrally based remote sensing of river bathymetry. Earth Surf Processes Landf 34, 1039–1059. https://doi.org/10.1002/esp.1787
27. Malone, T.C., Newton, A., 2020. The Globalization of Cultural Eutrophication in the Coastal Ocean: Causes and Consequences. Front. Mar. Sci. 7, 670. https://doi.org/10.3389/fmars.2020.00670
28. Manzo, C., Braga, F., Zaggia, L., Brando, V.E., Giardino, C., Bresciani, M., Bassani, C., 2018. Spatio-temporal analysis of prodelta dynamics by means of new satellite generation: the case of Po river by Landsat-8 data. International Journal of Applied Earth Observation and Geoinformation 66, 210–225. https://doi.org/10.1016/j.jag.2017.11.012
29. Matsushita, B., Yang, W., Chang, P., Yang, F., Fukushima, T., 2012. A simple method for distinguishing global Case-1 and Case-2 waters using SeaWiFS measurements. ISPRS Journal of Photogrammetry and Remote Sensing 69, 74–87. https://doi.org/10.1016/j.isprsjprs.2012.02.008
30. Mikhailova, M.V. (2002) 'The Hydrological Regime and the Peculiarities of Formation of the Po River Delta', Water Resources, 29(4), pp. 370–380.
31. Mishra, S., Mishra, D.R., 2012. Normalized difference chlorophyll index: A novel model for remote estimation of chlorophyll-a concentration in turbid productive waters. Remote Sensing of Environment 117, 394–406. https://doi.org/10.1016/j.rse.2011.10.016
32. Mohseni, F., Saba, F., Mirmazloumi, S.M., Amani, M., Mokhtarzade, M., Jamali, S., Mahdavi, S., 2022. Ocean water quality monitoring using remote sensing techniques: A review. Marine Environmental Research 180, 105701. https://doi.org/10.1016/j.marenvres.2022.105701
33. Niroumand-Jadidi, M., Bovolo, F., Bresciani, M., Gege, P., Giardino, C., 2022. Water Quality Retrieval from Landsat-9 (OLI-2) Imagery and Comparison to Sentinel-2. Remote Sensing 14, 4596. https://doi.org/10.3390/rs14184596
34. Niroumand-Jadidi, M., Legleiter, C.J., Bovolo, F., 2022b. River Bathymetry Retrieval From Landsat-9 Images Based on Neural Networks and Comparison to SuperDove and Sentinel-2. IEEE J. Sel. Top. Appl. Earth Observations Remote Sensing 15, 5250–5260. https://doi.org/10.1109/JSTARS.2022.3187179
35. Niroumand-Jadidi, M., Legleiter, C.J., Bovolo, F., 2025. Neural Network-Based Temporal Ensembling of Water Depth Estimates Derived from SuperDove Images. Remote Sensing 17, 1309. https://doi.org/10.3390/rs17071309

36. Niroumand-Jadidi, M., Gege, P., 2025. WASI-AI: Synergistic Integration of AI and Physics for Retrieving Water Quality and Benthic Parameters from Multi- and Hyperspectral Images. IEEE J. Sel. Top. Appl. Earth Observations Remote Sensing 18, 22832–22846. https://doi.org/10.1109/JSTARS.2025.3605061
37. Orlić, M., Kuzmić, M., Pasarić, Z., 1994. Response of the Adriatic Sea to the bora and sirocco forcing. Continental Shelf Research 14, 91–116. https://doi.org/10.1016/0278-4343(94)90007-8
38. Pahlevan, N., Schott, J.R., Franz, B.A., Zibordi, G., Markham, B., Bailey, S., Schaaf, C.B., Ondrusek, M., Greb, S., Strait, C.M., 2017. Sentinel-2 MultiSpectral Instrument (MSI) data processing for aquatic science applications: Demonstrations and validations. Remote Sensing of Environment 189, 261–271. https://doi.org/10.1016/j.rse.2016.11.026
39. Pahlevan, N., Smith, B., Alikas, K., Anstee, J., Barbosa, C., Binding, C., Bresciani, M., Cremella, B., Giardino, C., Gurlin, D., Fernandez, V., Jamet, C., Kangro, K., Lehmann, M.K., Loisel, H., Matsushita, B., Hà, N., Olmanson, L., Potvin, G., Simis, S.G.H., VanderWoude, A., Vantrepotte, V., Ruiz-Verdù, A., 2022. Simultaneous retrieval of selected optical water quality indicators from Landsat-8, Sentinel-2, and Sentinel-3. Remote Sensing of Environment 270, 112860. https://doi.org/10.1016/j.rse.2021.112860
40. Politi, E., Cutler, M.E.J., Rowan, J.S., 2015. Evaluating the spatial transferability and temporal repeatability of remote-sensing-based lake water quality retrieval algorithms at the European scale: a meta-analysis approach. International Journal of Remote Sensing 36, 2995–3023. https://doi.org/10.1080/01431161.2015.1054962
41. Roy, D.P., Wulder, M.A., Loveland, T.R., C.E., W., Allen, R.G., Anderson, M.C., Helder, D., Irons, J.R., Johnson, D.M., Kennedy, R., Scambos, T.A., Schaaf, C.B., Schott, J.R., Sheng, Y., Vermote, E.F., Belward, A.S., Bindschadler, R., Cohen, W.B., Gao, F., Hipple, J.D., Hostert, P., Huntington, J., Justice, C.O., Kilic, A., Kovalskyy, V., Lee, Z.P., Lymburner, L., Masek, J.G., McCorkel, J., Shuai, Y., Trezza, R., Vogelmann, J., Wynne, R.H., Zhu, Z., 2014. Landsat-8: Science and product vision for terrestrial global change research. Remote Sensing of Environment 145, 154–172. https://doi.org/10.1016/j.rse.2014.02.001
42. Vanhellemont, Q., Ruddick, K., 2018. Atmospheric correction of metre-scale optical satellite data for inland and coastal water applications. Remote Sensing of Environment 216, 586–597. https://doi.org/10.1016/j.rse.2018.07.015
43. Vanhellemont, Q., Ruddick, K., 2021. Atmospheric correction of Sentinel-3/OLCI data for mapping of suspended particulate matter and chlorophyll-a concentration in Belgian turbid coastal waters. Remote Sensing of Environment 256, 112284. https://doi.org/10.1016/j.rse.2021.112284
44. Vona, I., Colella, S., Sammartino, M., Brando, V.E., Falcini, F., 2025. Positive correlation between the Po River discharge and ocean colour trends of Chl and TSM in the Adriatic Sea. Front. Remote Sens. 6, 1574347. https://doi.org/10.3389/frsen.2025.1574347

45. Warren, M.A., Simis, S.G.H., Martinez-Vicente, V., Poser, K., Bresciani, M., Alikas, K., Spyrakos, E., Giardino, C., Ansper, A., 2019. Assessment of atmospheric correction algorithms for the Sentinel-2A MultiSpectral Imager over coastal and inland waters. Remote Sensing of Environment 225, 267–289. https://doi.org/10.1016/j.rse.2019.03.018
46. Zhang, S., Wang, D., Gong, F., Xu, Y., He, X., Zhang, X., Fu, D., 2023. Evaluating Atmospheric Correction Methods for Sentinel−2 in Low−to−High−Turbidity Chinese Coastal Waters. Remote Sensing 15, 2353. https://doi.org/10.3390/rs15092353

# Appendix A Detailed Match-up Dataset Statistics

*Table A.1 Summary of match-up dataset sizes for training and validation across sensor platforms, atmospheric processing levels, water quality parameters, and monitoring sites.*

| Sensor | Product | Parameter | Site | N (Train) | N (Val) |
|---|---|---|---|---|---|
| Sentinel-2 MSI | TOA | Chl-a | Probe E1 | 177 | 30 |
| | | | Probe S1 | 178 | 43 |
| | | | Total | 355 | 73 |
| | | Turbidity | Probe E1 | 175 | 30 |
| | | | Probe S1 | 133 | 32 |
| | | | Total | 308 | 62 |
| | SR | Chl-a | Probe E1 | 149 | 21 |
| | | | Probe S1 | 158 | 37 |
| | | | Total | 307 | 58 |
| | | Turbidity | Probe E1 | 148 | 21 |
| | | | Probe S1 | 115 | 28 |
| | | | Total | 263 | 49 |
| Landsat-8/9 OLI | TOA | Chl-a | Probe E1 | 48 | 30 |
| | | | Probe S1 | 58 | 43 |
| | | | Total | 106 | 73 |
| | | Turbidity | Probe E1 | 47 | 30 |
| | | | Probe S1 | 42 | 32 |
| | | | Total | 89 | 62 |
| | SR | Chl-a | Probe E1 | 56 | 21 |
| | | | Probe S1 | 59 | 37 |
| | | | Total | 115 | 58 |
| | | Turbidity | Probe E1 | 55 | 21 |
| | | | Probe S1 | 46 | 28 |
| | | | Total | 101 | 49 |

*Note: N denotes the number of match-up samples. 'Train' and 'Val' refer to the datasets used for model training and validation, respectively.*